



Michigan Technological University
Create the Future Digital Commons @ Michigan Tech

Dissertations, Master's Theses and Master's
Reports - Open

Dissertations, Master's Theses and Master's
Reports

2011

Processing and mechanical properties of cast aluminum containing scandium, zirconium, and ytterbium

Nicholas D. Johnson
Michigan Technological University

Follow this and additional works at: <https://digitalcommons.mtu.edu/etds>


 Part of the [Engineering Science and Materials Commons](#)

Copyright 2011 Nicholas D. Johnson

Recommended Citation

Johnson, Nicholas D., "Processing and mechanical properties of cast aluminum containing scandium, zirconium, and ytterbium ", Master's Thesis, Michigan Technological University, 2011.
<https://doi.org/10.37099/mtu.dc.etds/28>

Follow this and additional works at: <https://digitalcommons.mtu.edu/etds>

 Part of the [Engineering Science and Materials Commons](#)

PROCESSING AND MECHANICAL PROPERTIES OF CAST ALUMINUM
CONTAINING SCANDIUM, ZIRCONIUM, AND YTTERBIUM

By

Nicholas D. Johnson

A THESIS

Submitted in partial fulfillment of the requirements for the degree of

MASTER OF SCIENCE

(Materials Science and Engineering)

MICHIGAN TECHNOLOGICAL UNIVERSITY

2011

©2011 Nicholas Johnson

This thesis, "Processing and Mechanical Properties of Cast Aluminum Containing Scandium, Zirconium, and Ytterbium," is hereby approved in partial fulfillment of the requirements for the Degree of MASTER OF SCIENCE IN MATERIALS SCIENCE AND ENGINEERING

Department of Materials Science and Engineering

Signatures:

Thesis Advisor

Dr. Paul G. Sanders

Committee Member

Dr. Stephen Kampe

Committee Member

Dr. Scott Miers

Department Chair

Dr. Mark R. Plichta

Date

To my parents Cheri Marchio and Dave Johnson for their guidance, support, and love.

Table of Contents

Table of Contents	4
List of Figures	6
List of Tables	8
Acknowledgements	9
Abstract	10
1. Introduction	11
1.1 Aluminum Alloying and Strengthening	11
1.2 Aluminum Alloys Containing Scandium	13
1.3 Scandium Recovery	14
1.4 Scandium Strengthening, and Ternary and Quaternary Additions	15
1.5 Mechanical Properties	17
2. Goals and Hypotheses	19
3. Methods	20
3.1 Cast Samples	20
3.2 Crucible-Melt Interaction Study	21
3.3 Composition Determination	23
3.4 Heat Treatment Optimization	24
3.5 Ultrasonic Measurements	25
3.6 Tensile Bars	27
4. Results and Discussion	31
4.1 Cast Samples	31
4.2 Crucible-Melt Interaction Study	39
4.3 Composition Determination	42
4.4 Heat Treatment Optimization	43
4.5 Ultrasonic Measurements	47
4.6 Tensile Bars	50
5. Future Work	62
6. Conclusions	63
7. References	64

8. Appendix A.....	66
--------------------	----

List of Figures

Figure 1.1: The Aluminum rich side of the Al-Sc phase diagram. (3)	13
Figure 1.2: The aluminum rich Al-Zr phase diagram. (12)	16
Figure 3.1: Crucibles sectioned and mounted for WDS analysis, where the red lines indicate the positions of the WDS line scans.....	22
Figure 3.2: A casting produced from the ASTM B-108 tensile bar mold. Two tensile bars are produced from each casting, and once removed from the gating and riser require no further machining.	27
Figure 3.3: A casting produced from the cylinder bar mold. Four tensile samples are produced from each casting, and require machining before they can be tested. ..	28
Figure 3.4: Thermocouple positions in the cylinder mold for measuring mold and melt temperatures during casting. The cylinders are 0.75 in (19mm) diameter and 7.5 in (109.5 mm) long.	29
Figure 4.1: Predicted porosity in the tensile bar mold when cast at 800 °C and at a mold preheat of 400 °C using an Al-0.5Si alloy. Solid casting is light blue, porosity is red, orange, yellow and white in increasing order of severity.	32
Figure 4.2: Observed porosity in tensile bars cast in the ASTM B-108 mold. Observe the large amount of porosity in the lower grip extending into the gage section, which agrees well with the simulation above.	32
Figure 4.3: The red circle shows a small crack near the upper grip of a tensile bar that has been heat treated but not pulled. The crack is a result of hot tearing in the mold.	33
Figure 4.4: The new mold design, with the sprue in the center, creates 4 cylinders per casting which can be machined into tensile bars. The bar diameter is slightly larger than the finished grip diameter of 0.625 in (16 mm).....	34
Figure 4.5: MAGMASoft simulation of the new mold at room temperature being filled with 760 °C AlSi05 showing porosity at the bottoms of the cylinders and typical cone shrinkage porosity at the top of the cylinders and in the pouring basin.	34
Figure 4.6: Experimental and simulated temperatures of thermocouples 1, 2 and 4 during a pour in the cylinder bar mold.	36
Figure 4.7: Experimental and simulated temperatures in the cylinder mold for thermocouples 6-9 during casting. Thermocouples 8 and 9 were monitoring mold temperature.	37
Figure 4.8: Scandium concentrations at points along WDS line scans where point 1 represents the inside edge of the crucible, and point 10 being nearest the outside edge. For simplicity, only the scans on the sides of a crucible are shown, but are representative of the scans across the bottom for the same crucible type. Solid horizontal lines represent the minimum detectable limit (MDL) of Sc for each crucible. The overall composition of the melt was 1.0 at. % Sc.....	39
Figure 4.9: The four crucibles after solidification and sectioning showing convex menisci and a lack of wetting between the crucible and the melt.	40

Figure 4.10 (top) and Figure 4.11 (bottom): Isochronal aging performed from 150 to 500 °C on samples of 4 different compositions. Non Sc containing samples clearly exhibit peak aging at 150 °C, where the Sc containing alloys exhibit peak aging at 350 °C. Conductivity increases as solute atoms precipitate out of solution, and eventually decreases again as precipitates break down to allow others to coarsen, increasing solute atoms in solution.	44
Figure 4.12 (top) and Figure 4.13 (bottom): Isochronal aging performed from 150 °C to 500 °C on samples of 4 different compositions. Al-0.03Zr at. % exhibits a weak peak at 150 °C, while the Sc containing alloys all exhibit peak aging at 350 °C. Conductivity increases when solute atoms precipitate out of solution around 200 °C, and eventually decreases again as precipitates break down to allow others to coarsen, increasing solute atoms in solution.	46
Figure 4.14: Samples after polishing and etching for grain size measurements. From left to right, alloy 5, 6, 7, and 8(1). The grains get smaller in size from left to right.	47
Figure 4.15: Main effects plot of alloying additions on the elastic modulus (in GPa).	49
Figure 4.16: Main effects plot of alloying additions on yield strength.	51
Figure 4.17: Main effects plot of alloying additions on UTS.	52
Figure 4.18: Main effects plot of alloying additions on elongation.	53
Figure 4.19: Boxplot of the yield strength of alloys 4 and 6.	56
Figure 4.20: Boxplot of the UTS of alloys 4 and 6.	57
Figure 4.21: Boxplot of the elongation values exhibited by alloys 4 and 6.	58
Figure 4.22: Tensile bars exhibiting the four failure modes. Tensile bars were from alloys 5, 8, 4, and 6 from left to right. <i>A</i> indicates a cone-cup type fracture, and <i>B</i> indicates a 45 degree plane type fracture. The bars on the outside did not fracture entirely, the two on the inside fractured completely.	60

List of Tables

Table 1.1 Values of the Gibbs free energy in J/mol of the reaction for Sc or Al to reduce crucible types	15
Table 3.1 Crucible diameters and fill amounts	21
Table 3.2 Standards used for calibration and the elements that were calibrated for	22
Table 3.3 Concentrations in mg/L of standards used in calibration for ICP-OES	24
Table 3.4 Nominal compositions in at. % of alloys used in isochronal aging study, balance is aluminum	25
Table 3.5 Pouring temperatures and number of pours of alloys cast in the cylinder bar mold	30
Table 4.1 Results of the ICP composition measurements in at. %	42
Table 4.2 Impurities present in the 99.99% Al master alloy	42
Table 4.3 Yield of elements added to alloys	43
Table 4.4 Grain size of alloys 5-8 as cast	47
Table 4.5 Results of the ultrasonic measurement of elastic modulus and Poisson's ratio	48
Table 4.6 Results of tensile testing alloys 1-8	50
Table 4.7 The precipitate radii found for various alloys and heat treatments	54
Table 4.8 Expected Orowan strengthening values in MPa for 2.5, and 4 nm radius particles for each Sc containing alloy, and observed hardness and UTS increases for the same alloys	55
Table 4.9 Fracture surface geometry of the tensile samples	60

Acknowledgements

I would like to thank the following people for their contributions to this work

Kyle Deane for his work with MAGMASOFT and mold modeling
Austin DePottey for help with the heat treatment optimization study
Jennifer Eikenberry for ICP analysis
Michel Knudsen for mold modeling and machining
Ruth Kramer for assistance with sample preparation
Ed Laitila for assistance with ultrasonic testing
Owen Mills for SEM WDS measurements
Pat Quimby for assistance with melting and casting
Lance Taylor for assistance with the heat treatment optimization study
Mark Twilley for his work with MAGMASOFT and mold modeling
Tom Wood for assistance with mold design

In addition I would like to thank my fellow graduate students Justin Clark, Meghan Haycock, and Joe Licavoli for all of their intellectual support with my work.

I would like to thank David Dunand, David Seidman, and Christopher Booth-Morrison at Northwestern University for their contributions.

I would also like to thank Ford Motor Company and GS Engineering for their generous financial support that allowed for this work to be performed.

Abstract

A series of aluminum alloys containing additions of scandium, zirconium, and ytterbium were cast to evaluate the effect of partial ytterbium substitution for scandium on tensile behavior. Due to the high price of scandium, a crucible-melt interaction study was performed to ensure no scandium was lost in graphite, alumina, magnesia, or zirconia crucibles after holding a liquid Al-Sc master alloy for 8 hours at 900 °C in an argon atmosphere. The alloys were subjected to an isochronal aging treatment and tested for conductivity and Vickers microhardness after each increment. For scandium-containing alloys, peak hardnesses of 520-790 MPa, and peak tensile stresses of 138-234 MPa were observed after aging from 150-350 °C for 3 hours in increments of 50 °C, and for alloys without scandium, peak hardnesses of 217-335 MPa and peak tensile stresses of 45-63 MPa were observed after a 3 hour, 150 °C aging treatment. The hardness and tensile strength of the ytterbium containing alloy was found to be lower than in the alloy with no ytterbium substitution.

1. Introduction

1.1 Aluminum Alloying and Strengthening

Aluminum alloys have traditionally been employed in weight sensitive applications or other situations where a high specific strength is necessary, such as aerospace, sporting equipment, and increasingly as a part of ground transportation. Many conventional Al alloys are available with high strength and/or ductility, however many of these alloys lose their strength rapidly at temperatures above $0.54 T_m$ (230 C). This strength loss is attributable to overaging of the secondary strengthening phases in these alloys in addition to annealing effects. Attempts to improve high temperature strength of Al alloys have been made for more than three decades because aluminum possesses several attributes which are favorable for high temperature applications (1). Aluminum based alloys for high temperature applications have many desirable characteristics, such as comparative low cost relative to Ni- or Ti-based alloys, oxidation resistance, and a face-centered cubic (FCC) unit cell which is more creep resistant than other less highly packed unit cells (1). The other key benefit of Al is its comparatively low density and high strength to weight ratio.

Traditionally, high strength aluminum alloys have relied on precipitate strengthening, solute strengthening, strain hardening, and grain size strengthening either individually, or in combination with each other. In precipitate hardened alloys, smaller precipitates are usually sheared by dislocations, while larger precipitates are bypassed by an Orowan dislocation looping mechanism. At room temperature, dislocation climb over precipitates is not a significant contributing factor due to the lack of available thermal energy for dislocations to climb out of their glide plane. Solute strengthening is a mechanism by which solute atoms in the matrix create strains in the matrix resulting in restriction of dislocation motion. This effect is due to the difference in sizes and moduli of the solute and matrix atoms. Strain hardening occurs after a ductile material has been deformed. As a material is deformed, dislocations are generated, and the overall dislocation density increases. As the density of dislocations increases, it becomes increasingly difficult to move existing dislocations or generate new dislocations. Grain size strengthening, or Hall-Petch strengthening, occurs as the grain size is reduced. Smaller grains have a greater surface area per unit volume than larger grains. Because grain boundaries are barriers that impede dislocation motion, the greater amount of grain boundaries present in a material with smaller grains will increase the overall resistance to dislocation motion, which results in a strengthening effect in the material. The relative importance of each of these mechanisms depends on the system they are in, however usually grain size strengthening is a weaker effect when compared to precipitate or solute strengthening. Strain hardening is not always a viable strengthening mechanism because plastic deformation is required for strain hardening. In some material processes like casting, plastic deformation would be performed after solidification, but most products are cast to

near net shape, so any plastic deformation would result in additional machining or other processing time to achieve net shape.

Orowan strengthening in Al can be calculated using equation 1.1

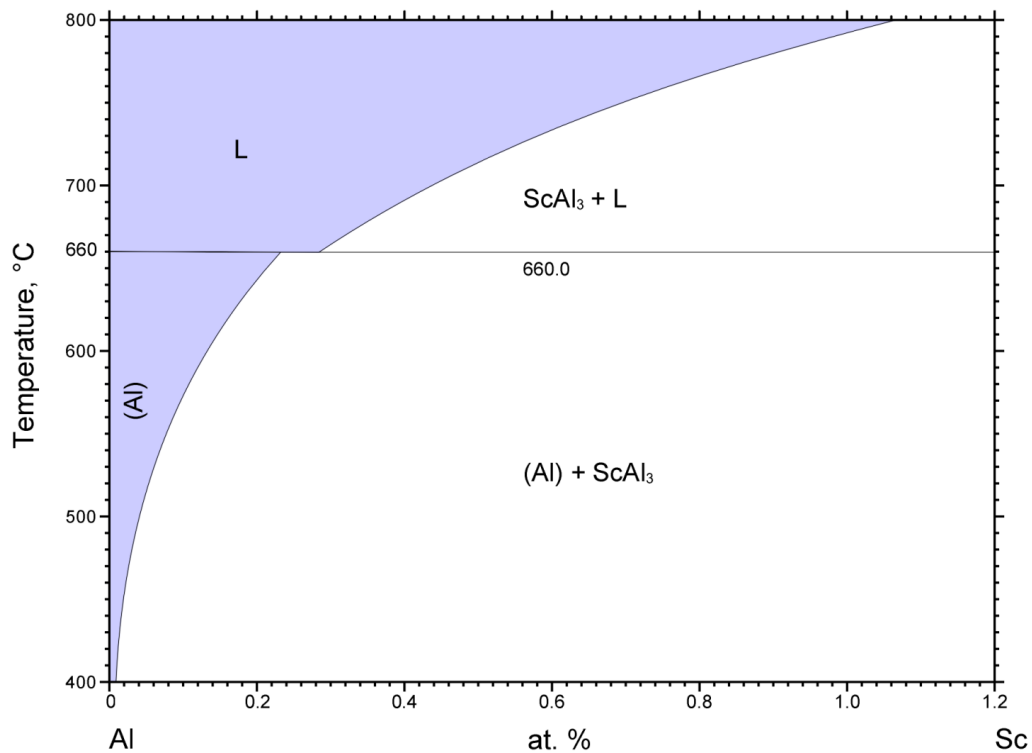
$$\Delta\sigma_{or} = M * \frac{0.4 * G_{Al} * b}{\pi\sqrt{1-\nu}} * \frac{\ln(\frac{2\bar{R}}{b})}{\lambda_{e-e}} \quad \text{eq. 1.1}$$

The change in strength is represented by $\Delta\sigma_{or}$, M is the mean Taylor orientation factor, G_{Al} is the shear modulus of aluminum, b is the magnitude of the Burgers vector for pure aluminum, ν is the Poisson's ratio for pure aluminum, $\bar{R} = \frac{\pi}{4} \langle R \rangle$ is the mean precipitate planar radius, $\langle R \rangle$ is the mean particle radius, and the edge to edge inter precipitate

spacing is estimated as $\lambda_{e-e} = \left(\sqrt{\frac{2\pi}{3\phi}} - \frac{\pi}{2} \right) \langle R \rangle$, ϕ is the particle volume fraction (2).

1.2 Aluminum Alloys Containing Scandium

The use of Sc as a strengthener for Al alloys has been explored extensively, as Sc has many characteristics that make it a very effective strengthener in Al. Al_3Sc forms a eutectic with Al at a composition of Al-0.28 at. % Sc, and on the hypoeutectic side, there is an extremely narrow temperature range ($<1^\circ\text{C}$) over which the liquid-solid two phase region exists, allowing for rapid solidification and supersaturation of the resulting solid. Rapid solidification is important in casting alloys for minimizing the effect of shrinkage porosity by distributing it more evenly. Furthermore, the decrease in solid solubility of Sc in Al from 0.23 at. % at the eutectic temperature down to below 0.01 at. % at 400°C allows for easy precipitation of Al_3Sc from Al in subsequent aging. Upon decomposition from the Al-Sc supersaturated solution, fine, evenly dispersed Al_3Sc precipitates nucleate. These precipitates have an L_{12} crystal structure and are coherent with the Al matrix up to precipitate radii of at least 15 nm (2). Orowan strengthening is the primary mechanism for precipitate strengthening above a 3 nm radius in Al-Sc alloys (2). Figure 1.1 shows the Al rich portion of the Al-Sc phase diagram.



© ASM International 2009. Diagram No. 100032

Figure 1.1: The Aluminum rich side of the Al-Sc phase diagram. (3)

The maximum solubility of Sc in Al is highly sensitive to the cooling rate at which the alloy was solidified. Under a cooling rate of 10^7 K/s solubilities of up to 3.2 at. % have been reported (6), however under more conventional casting solidification rates of 1-100 K/s solubilities of 0.24-0.3 at. % have been reported (4). It is also possible to get grain refinement from primary Al_3Sc precipitates when hypereutectic compositions above 0.36 at. % Sc are used (4). The primary Al_3Sc precipitates act as heterogeneous nucleation sites for solidifying α -Al grains (2). These precipitates can also provide recrystallization resistance by the Zener drag mechanism, where grain boundaries are pinned in place due to lower energies associated with particles interfacing with the grain boundary, rather than generating a new interface which would raise the overall energy of the system (5). The presence of the precipitates limits the size of the new grains, but does not inhibit the nucleation of new grains directly.

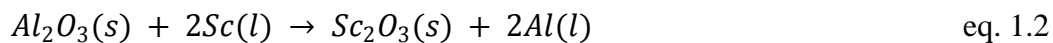
1.3 Scandium Recovery

Several commercial aluminum alloys that contain scandium exist, and some new alloys are being developed that contain additions of scandium. With the price of scandium in excess of \$5400/kg (7), it is important maximize scandium recovery. Two possible sources of losses are to oxidation and crucible-melt interactions. It is therefore important to study the reaction of an aluminum-scandium master alloy with various common crucible types to determine the optimal crucible type for minimizing losses, and also to develop a casting method that minimizes oxidation of scandium.

One method for minimizing any oxidation reactions of the melt is the use of an inert cover gas such as Ar. Because Ar is more dense than oxygen, if flowed over the melt it will displace the oxygen, thus reducing the possibility of oxidation due to the lack of oxygen that is able to come into contact with the melt.

Previous studies have examined the reaction between various melt and crucible types, focusing on nickel and titanium alloys, where losses are expensive and reactions are prevalent (8,9). An important consideration in choosing a crucible for a certain melt type involves the contact angle that the melt will make with the chosen crucible type. A crucible-melt pair where the melt does not wet the crucible will give less opportunity for the melt and crucible to react. Wetting enables thorough contact between the crucible and the melt, thereby allowing reactions to more easily take place. After solidification, if the meniscus of the solid is concave, this indicates wetting, and therefore a greater possibility of a reaction.

Gibbs free energy calculations can be performed to see if the reaction of Sc reducing a crucible is one that is possible spontaneously. An example reaction is equation 1.2



According to these calculations, Sc should reduce alumina, magnesia, and zirconia crucibles. The calculations can also be performed for Al reducing the crucibles, in the case that the crucibles are filled with an Al-Sc master alloy, Table 1.1 shows the results of these calculations at 1173 K or 900 °C. The calculations indicate that Sc should reduce the crucibles preferentially compared to Al.

Table 1.1

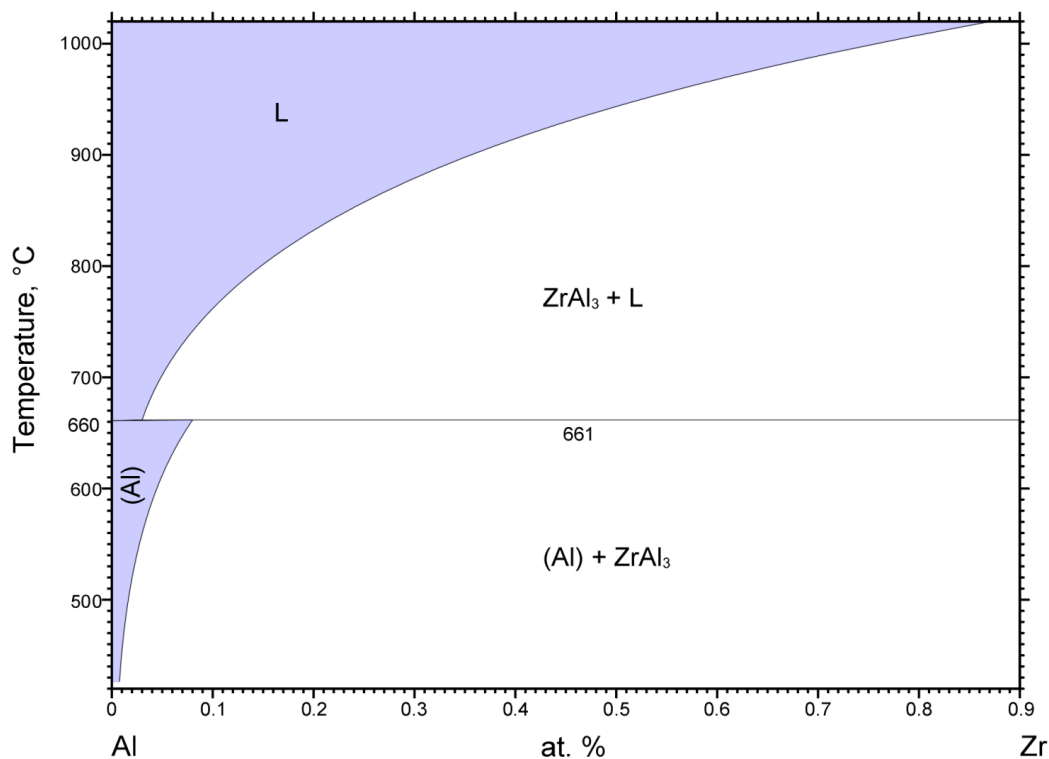
Values of the Gibbs free energy in J/mol of the reaction for Sc or Al to reduce crucible types

Crucible	ΔG of Sc reduction reaction	ΔG of Al reduction reaction
Alumina	-2.317×10^5	-
Magnesia	-1.385×10^5	-1.75×10^4
Zirconia	-4.808×10^5	$+9.315 \times 10^4$

1.4 Scandium Strengthening, and Ternary and Quaternary Additions

Not only does Sc serve as a very potent strengthener for Al, with strengthening values of 1000-1460 MPa per at% reported (10,11), but it also retains this strengthening at elevated temperatures up to 300 °C before significant coarsening of the precipitates occurs resulting in a loss of strength. The use of several other elements in addition to Sc have been studied, with Zr showing one of the best synergistic effects (2,4,5,11). Zr has a much lower diffusivity in Al compared to Sc, so it is possible to precipitate out the Al_3Sc precipitates, and then subsequently increase the heat treatment temperature to allow the Zr to diffuse to the precipitates. Unlike Al_3Sc , the equilibrium structure of Al_3Zr is DO_{23} , but the metastable $L1_2$ phase will form an $Al_3(Sc_{1-x}Zr_x)$ precipitate where up to half of the Sc atoms can be replaced by Zr (1). Typically the Zr atoms are distributed as a shell around the core Al_3Sc precipitate in Al-Sc-Zr alloys due to the slower diffusivity of Zr. Because the diffusivity of Sc in Al_3Zr is much lower than in Al, the Al_3Zr shell that forms around the Al_3Sc precipitates serves to significantly slow down the coarsening of the precipitates at elevated temperatures. Also, the increased overall solute content creates a higher overall volume fraction of precipitates, yielding higher strength values. Zirconium additions to Sc create stronger alloys that have improved high temperature coarsening resistance. Al_3Sc and Al_3Zr precipitates are also thermodynamically stable due to their high melting temperatures of 1280 °C and 1580 °C respectively.

Zr on its own is not suitable as the primary strengthening mechanism in Al alloys however, for several reasons. First, Al_3Zr forms a peritectic with $\alpha\text{-Al}$ (Figure 1.2), which creates a high segregation of Zr in the alloy, with most of the Zr being concentrated at the center of the dendrites in the first to solidify regions, and the interdendritic regions being nearly Zr free. If such an alloy is precipitation hardened, there will be large precipitate free zones in the interdendritic area, which have been shown to be highly detrimental to overall strength (2). It is also not possible to homogenize Al-Zr alloys, because doing so will create the DO_{23} equilibrium precipitates which are not coherent with the matrix, rather than create the metastable, coherent L_{12} precipitates. Finally, the strengthening effect from Zr has been shown to be less than half that of Sc on a per atom basis (2,11).



© ASM International 2006. Diagram No. 1600336.

Figure 1.2: The aluminum rich Al-Zr phase diagram. (12)

The eutectic nature of the equilibrium between Al_3Sc and $\alpha\text{-Al}$ creates a distribution of Sc that is opposite to the distribution of Zr, with more of the Sc being segregated to the

interdendritic regions, and with the core of the dendrites being slightly Sc poor. The extent of the segregation is not as high as for Zr however, with Zr concentration being nearly doubled in the center of dendrites, and nearly zero in the interdendritic zones, Sc concentration is only about 50% higher in the interdendritic zones, and 50% less in the dendrite cores (2,11).

Other elements that have been explored for ternary or quaternary addition to Al-Sc or Al-Sc-Zr alloys include Ti, Hf, Er, Tm, Yb, and Lu (1). These elements have been explored for their abilities to also sit on the Sc site in Al_3Sc precipitates, in addition to other characteristics such as ability to be conventionally cast, as well as low diffusivities to decrease coarsening kinetics. Of these, Yb stands out due to the eutectic nature of the equilibrium between Al_3Yb and $\alpha\text{-Al}$, and also due to the comparatively high solid solubility of 0.18 at. %, and the low solubility at heat treatment temperatures of < 0.1 at. % compared to nearly zero in both cases for the other elements that form eutectics. This low solubility level at heat treatment temperatures allows for a larger portion of the solute atoms to be precipitated out, and the high solubility at the eutectic temperature allows for a higher volume fraction of precipitates. Also attractive is Yb's low cost of just \$360/kg compared to Sc at \$5420/kg (7,13). Ytterbium possesses a higher diffusivity in Al than Sc, so alloys made from Al-Yb-Sc-Zr and subsequently precipitation hardened typically possess three layer cored precipitates, consisting of Al_3Yb at the center, surrounded by Al_3Sc , which is then covered with a layer of Al_3Zr (14).

1.5 Mechanical Properties

When developing a heat treating procedure for precipitation hardened alloys, a common practice is to measure hardness and conductivity to evaluate the reactions taking place. The heat treating practice that creates the maximum hardness is usually desired because harder materials are usually stronger materials. Conductivity of an alloy is dependent on many factors. One factor that affects conductivity is the presence of solute atoms. As the amount of solute atoms present in solution increases, the overall conductivity of the alloy will decrease (2). As these solute atoms precipitate out of solution, the conductivity of the alloy will correspondingly increase.

Many previous studies on these materials have focused on simply evaluating hardness and conductivity as a means of studying the characteristics of the materials after various heat treatments. Very few studies have produced samples of a large enough scale to produce tensile data, and instead have relied on compression studies and small creep samples for mechanical properties assessments (2,10,11). While tensile properties can be estimated from these other tests, it is still valuable to actually characterize the tensile behavior of these alloys, especially since so little information exists in the literature. Also, smaller scale tests used to characterize these materials are not as flaw sensitive as tensile testing, nor do they give data about tensile elongation, both of which are useful engineering parameters.

The modulus determined from tensile testing is not always an accurate representation of the true elastic modulus of a material due to machine compliance and porosity or other defects present in the samples; however, the use of ultrasonic measurements is a method commonly used to get more accurate measurements of this property. Ultrasonic measurements are performed by placing a transducer on the sample surface. The transducer produces a sound wave that travels from the top surface, through the sample, bouncing off the bottom surface, and returns to the transducer. This signal is then interpreted on an oscilloscope where the time that it takes the wave to travel down and back is measured. This time can be used in conjunction with a measurement of the sample thickness to calculate the speed of sound in the material. To ensure accurate measurements, the sample faces must be parallel, and should be smooth. If the surfaces are rough or non-parallel, then error is introduced into the velocity calculation. Equation 1.3 shows how to calculate the speed of the wave in the sample,

$$v = \frac{2t}{\text{time}} \quad \text{eq. 1.3 (15)}$$

where v is the speed, t is the thickness of the sample, and time is the round trip time for the wave.

Two transducers are used to measure sound waves, one measures the longitudinal wave, and another measures a transverse wave. Once the transverse (v_t) and the longitudinal (v_l) speeds are known, Poisson's ratio can be calculated. Equation 1.4 is used to determine Poisson's ratio.

$$\nu = \frac{1 - 2(v_t / v_l)^2}{2 - 2(v_t / v_l)^2} \quad \text{eq. 1.4 (15)}$$

Equation 1.5 can be used to calculate the elastic modulus once the velocities and the Poisson's ratio are known.

$$E = \frac{v_l^2 \rho (1 + \nu)(1 - 2\nu)}{1 - \nu} \quad \text{eq. 1.5 (15)}$$

Equation 1.6 can be used to calculate the shear modulus using the transverse velocity and the density.

$$G = v_t^2 \rho \quad \text{eq. 1.6 (15)}$$

2. Goals and Hypotheses

The goals of this thesis were to evaluate the castability of an Al-Sc-Zr-Yb alloy on a laboratory foundry scale of ca. 7-10 kg (15-20 lbs) at a time, to determine the tensile properties of such an alloy, and to develop a method for casting such an alloy, while considering possible sources of Sc loss.

Hypotheses:

1. Sc will be lost to common crucible types during melting, as supported by Gibbs free energy calculations.
2. Yb can be substituted for some Sc in an Al-Sc-Zr alloy to maintain the strength while decreasing the cost, because Yb will substitute for Sc in Al_3Sc precipitates producing comparable strength.

3. Methods

3.1 Cast Samples

Melting was performed using a 7-10 kg (15-20 lb) induction furnace. A graphite crucible was used, functioning as a susceptor. Thesuscepting crucible was found to retain heat in the melt longer when the furnace was turned off compared to a standard alumina crucible. This retention of heat is beneficial as the furnace must be turned off for pouring, and a crucible that removes more heat from the melt will require more reheating before the next pour compared to a crucible which retains heat. Melting practice involved first melting the 99.99 % Al ingot in the furnace. Once the ingot was melted, the master alloy(s) were added. After addition of the master alloy(s), the temperature of the melt was increased to 900 °C. This was done to help promote full melting and dissolution of the master alloy additions. Due to both the high temperature capability and the stirring effect from induction melting, dissolution was quick and thorough. After reaching 900 °C, the melt was allowed to cool to the pouring temperature. Casting was performed by pouring directly out of the furnace into the mold.

During the entire melting process, 99.99 % purity Ar cover gas was flowed into the top of the furnace at a flow rate of 2.4 L/min (5 SCFH). All melts that were poured into the cylinder mold were degassed. Degassing was performed with the induction power off using a rotary degasser, which consisted of a rotating lance that was immersed in the melt. Argon of 99.99 % purity was flowed through the lance at a flow rate of 2.4 L/min (5 SCFH). Degassing was performed for a total of 5 minutes. Melts that were degassed were done so after the initial melting and prior to the addition of any master alloy(s). Prior to degassing, the temperature of the melt was increased to 850 °C to allow for cooling during the degassing process so solidification during degassing could be avoided while the furnace was turned off.

3.2 Crucible-Melt Interaction Study

Because of the expected loss of Sc to the alumina, magnesia, and zirconia crucibles, a crucible-melt interaction study was performed. A non-oxide, graphite crucible was also selected for investigation. The four crucible compositions selected for this study are commonly used as crucibles in induction furnaces and are commercially available. It was not possible to obtain all four crucibles in the exact same size and geometry, so the crucibles were filled with a mass of master alloy that would result in them being filled to a depth of one half of the diameter of the crucible. The master alloy used for this study is Al 1.0 at. % Sc (NT Ruddock, Cleveland). Table 3.1 shows the four crucibles used for this study, as well as their diameters and the mass of Al-Sc master alloy that they were filled with.

Table 3.1
Crucible diameters and fill amounts

	Inner Diameter (mm)	Mass of master alloy (g)
Alumina	17.5	5.65
Zirconia	22.2	11.6
Magnesia	20.6	9.32
Graphite	36.5	51.6

A tube furnace was used for this study so the atmosphere could be controlled during the experiment. A preliminary experiment conducted in a box furnace with no atmospheric control resulted in severe oxidation of the master alloy that prevented interaction of the melt with the crucible.

The tube furnace was set to 900 °C and allowed to equilibrate for two hours. A temperature profile was taken of the furnace to determine the temperature inside the tube. The center of the hotspot was recorded at 884 °C, with the temperature falling to 860 °C within 3 inches (75 mm) on either side of the hot spot. After this, the furnace was allowed to cool, and was filled with samples. The four samples were loaded into the furnace, centered on the hot spot and extending about 2.5 inches (63 mm) on either side of the center, and then the furnace was sealed and turned on. 99.99% argon gas was flowed through the tube at a rate of 7 L/min during the entire heating, melting, and cooling process. The rate was selected to achieve 4 volume changes per minute and an inert atmosphere was assumed. The samples were heated for 8 hours, and then left to cool slowly in the furnace. This test was meant to be a worst case scenario, so the time and temperature were selected because they are significantly longer than any melt would ever be held in the crucible during normal casting procedures, and the highest temperature attained during normal melting for this alloy respectively.

After the samples cooled, they were sectioned in half vertically. If the master alloy could be removed, it was.

The mounts were then polished, and carbon coated, and then the crucibles were examined in a JEOL JXA-6400 scanning electron microscope (SEM) and analyzed with wavelength dispersive spectrometry (WDS). Figure 3.1 shows the mounts as prepared for WDS.

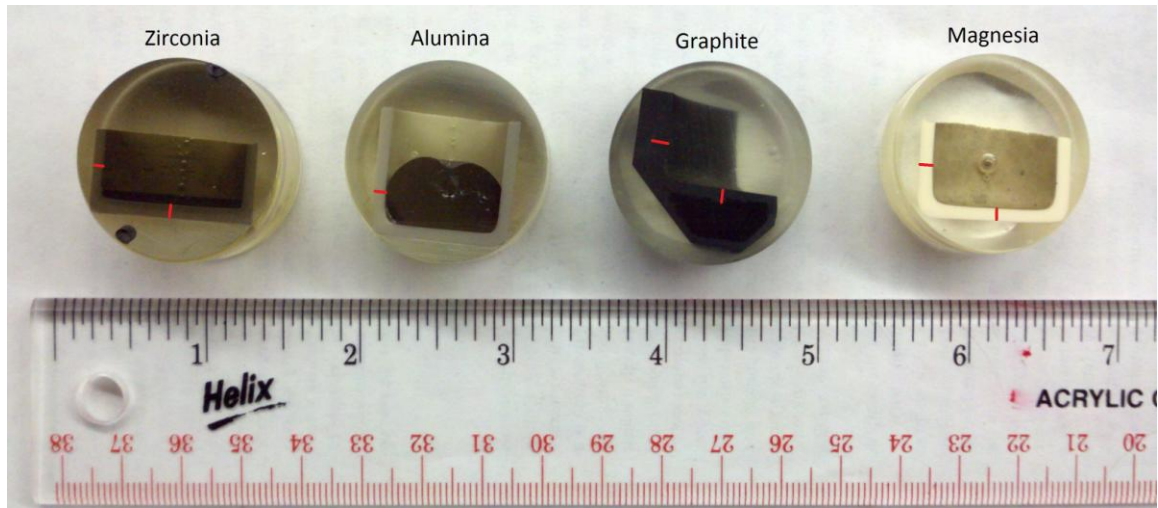


Figure 3.1: Crucibles sectioned and mounted for WDS analysis, where the red lines indicate the positions of the WDS line scans.

Before the mounts could be analyzed, the WDS system first had to be calibrated. A preliminary qualitative Electron Dispersive Spectrometry (EDS) scan was performed on each sample to determine which elements to analyze for with WDS to look for impurities in the crucibles that needed to be accounted for, and therefore which to calibrate for. The EDS scan was performed using a 4Pi Analysis system with Revolution software, and an ultrathin window on the detector. The elements that were found were Al, Ca, Mg, Na, S, Sc, Si, Y, Zr. The lines used for WDS were the K lines for all elements except Y and Zr where the L lines were used to avoid interference with other elements. Table 3.2 shows the elements that were calibrated for and which standards were used for the calibration.

Table 3.2

Standards used for calibration and the elements that were calibrated for

Standard	Elements
KHBL (Hornblende)	Al, Ca, Mg, Na, Si
CaSO ₄	S
Sc	Sc
YAG	Y
Zr	Zr

The alumina crucible was 99.8 % Al₂O₃. The magnesia crucible was MgO with impurities of Al, Si, Ca, and Y. The zirconia crucible was ZrO₂ stabilized with magnesia, and the graphite crucible contained impurities of Na, Al, and S.

Quantitative WDS point analyses were taken at intervals along a line beginning at the outside edge of the crucible and ending at the inside edge of the crucible to look for any scandium losses to the crucible. In the case of the graphite crucible, which was significantly thicker than the other crucibles used in this study, the scan was taken from the half-way point across the side, to the inside edge, and from a quarter of the way through the bottom from the inside, to the inside edge. Geller MicroAnalytical dSpec 7 automation and dQuant 7 software was used to control and compute the results of the WDS analyses. WDS was performed under the following conditions: 20 KeV accelerating voltage, with a 20 nA beam current.

3.3 Composition Determination

Inductively coupled plasma (ICP) optical emission spectrometry (OES) is a method of measuring concentrations in the parts per million (ppm) range for elements present in an aqueous solution. Metallic solids can be prepared for analysis with ICP using digestion in a strong acid, commonly HCl, HNO₃, HF, or some combination of the three. The solution that the solids are dissolved in is referred to as the sample matrix. For the analysis, it is important to dilute the samples so that the elements of interest are at a concentration of roughly 10 ppm for ease of measurement. If the concentrations are too high, the intensity of the emission will be too high and can be difficult to accurately measure. The machine is calibrated using standards of known concentrations. A curve is then made by using several different concentrations of the standard, usually from 0.01 to 100 ppm. It is important that the measured solution fall within this range for the measurement to be accurate. A sample matrix with no dissolved solids should be used to prepare and dilute the standard solution for consistency.

To prepare a sample for ICP OES, first the sample was reduced to a fine size using mechanical cutting because smaller pieces allow for a faster digestion. A precision balance was used to weigh out 0.15 g of sample, and then the sample was placed in a plastic sample vial to avoid silicon contamination from glass. After being placed in the sample vial, 2.5 mL of 12.1 M HCl was added to the vial, followed by 1 mL of 70% HNO₃. Digestion of the sample was assisted by heating to 50 °C with the beaker covered using a watchglass, and stirring with a Teflon coated magnet. After digestion was complete, the vial was filled to 15 mL using DI water, and then capped and shaken thoroughly.

ICP-OES analysis was performed using a PerkinElmer ICP-OES, model 7000 DV. The RF Power was 1300 watts with a plasma gas flow rate of 15 L/min, auxiliary gas flow rate of 0.2 L/min, a nebulizer gas flow rate of 0.80 L/min, and a pump flow rate of 1.5 mL/min. Each sample was measured for the intensity of characteristic emission peaks, and then this intensity was compared against a calibration curve that was made from at least 3 points where the ends of the curve were at values above and below the value of the element in the solution. The points chosen for the calibration curve depended on the concentration of the elements tested for. Table 3.3 shows the concentrations of the

standards used for calibration. For alloys that contained Yb, standards 4-7 were used, and alloys that did not contain Yb used standards 1-3.

Table 3.3
Concentrations in mg/L of standards used in calibration for ICP-OES

	Std 1	Std 2	Std 3	Std 4	Std 5	Std 6	Std 7	Used
Sc	0.02510	0.05020	0.1004	1.004	5.020	15.06	30.12	4-7
Er	0.02510	0.05020	0.1004	1.004	5.020	15.06	30.12	1-3
Zr	0.02668	0.05335	0.1067	1.067	5.335	16.01	32.01	4-7
Si	0.02530	0.05060	0.1012	1.012	5.060	15.18	30.36	2-5
Yb	0.02560	0.05120	0.1024	1.024	5.120	15.36	30.72	1-3 or 4-7
Gd	0.02540	0.05080	0.1016	1.016	5.080	15.24	30.48	1-3
Yb	0.02710	0.05420	0.1084	1.084	5.420	16.26	32.52	1-3
Fe	0.02558	0.05115	0.1023	1.023	5.115	15.35	30.69	1-3
Ti	0.02565	0.05130	0.1026	1.026	5.130	15.39	30.78	2-5

3.4 Heat Treatment Optimization

An isochronal aging study was performed on samples of eight different compositions, shown in Table 3.4. The isochronal aging in air was performed for 3 hours with temperature intervals of 50 °C, starting at 150 °C up to 500 °C. After each aging temperature, the sample was water quenched, and then polished so 15 Vickers hardness tests could be performed across multiple grains on each sample, and a conductivity measurement taken. Vickers hardness testing was done with a load of 200 g for 15 s. Conductivity was measured by placing the probe of a Magnatest FM-100 eddy current conductivity tester flush with sample surface and recording the conductivity value. Only one measurement was performed on each sample.

Table 3.4

Nominal compositions in at. % of alloys used in isochronal aging study, balance is aluminum

Alloy	Sc	Zr	Yb
1	0	0	0.01
2	0	0	0.02
3	0	0.03	0.02
4	0.06	0.03	0.02
5	0	0.03	0
6	0.08	0.03	0
7	0.11	0.03	0
8	0.14	0.03	0

The compositions of alloys 1-3 were chosen to examine the effects of Yb and Zr on the tensile properties of Al. Alloy 4 was chosen to represent an Al-0.08Sc-0.03Zr at.% alloy where 0.02 at. % Sc had been replaced with 0.02 at. % Yb. Alloy 5 was an examination of the effect of just Zr on the tensile behavior. Alloy 6 was used as a comparison to the alloy where Yb was substituted. Alloys 7 and 8 were used to attempt to obtain grain refinement from higher Sc levels. To evaluate this, as cast samples of alloys 5-8 were metallographically polished, and then etched. Etching was performed by immersion in 0.3 M NaOH heated to 50 °C for 5 minutes. Due to the high anisotropy of the grains, grain size measurements were estimated by counting the number of grains on the surface of the sample, and dividing by surface area of the sample.

3.5 Ultrasonic Measurements

Ultrasonic measurements were performed on samples from all 4 compositions from both heats. The samples were sectioned out of the cylinders with parallel faces, and then polished with 600 grit abrasive paper to reduce the surface height variation. Transverse measurements were performed using molasses as a coupling agent, and longitudinal measurements used glycol gel. Each sample was measured three times for both longitudinal and transverse waves. The measurements were performed using a DSO-2250 PC-Oscilloscope and the DSO-2250 software. The transducers were shifted around

on the sample surface to identify peaks in the wave form that were reflections of the same peak. Once two peaks that were reflections of each other were found, the output was frozen using the software, and the distance between the peaks was measured using the software. The density each sample was measured using the Archimedes method. Using equations 1.3 through 1.6, the three time measurements in conjunction with the density and a thickness measurement using a calipers were used to calculate a value of the elastic modulus, shear modulus and Poisson's ratio for each of the three time measurements, and then the three values were averaged for a sample average for each material property.

3.6 Tensile Bars

An ASTM B-108 tensile bar mold was used to cast samples of several compositions in an initial trial. Figure 3.2 shows an example casting from the mold. Bars from an Al-0.06Sc-0.06Zr at. % alloy were cut from the gating, and then both bars were used to determine if there was an effect of homogenization on the mechanical properties of the bars. This was done by homogenizing one bar at 640 °C for 72 hours and then water quenching. After the homogenization, both bars were heat treated using a two-step aging process, where the bars are treated at 300 °C for 4 hours, and then finished at 425 °C for 8 hours. After this, they were then pulled at a strain rate of 10^{-4} /s, with an extensometer measuring strain.



Figure 3.2: A casting produced from the ASTM B-108 tensile bar mold. Two tensile bars are produced from each casting, and once removed from the gating and riser require no further machining.

Other tensile bars were produced from a second permanent mold. The second mold cast four cylinders rather than two tensile bars (Figure 3.3). The mold was fitted with several thermocouples in an attempt to monitor the temperature of the mold during casting, as well as to monitor the temperature of the casting during solidification and cooling to attempt to measure the cooling rate. Figure 3.4 shows the thermocouple positions in the mold. Thermocouples 5, 8, and 9 were placed in the mold, near the surface of the casting to monitor the mold temperature as casting progressed. The other thermocouples were placed in direct contact with the melt, protruding into the mold cavity by 1 mm.



Figure 3.3: A casting produced from the cylinder bar mold. Four tensile samples are produced from each casting, and require machining before they can be tested.

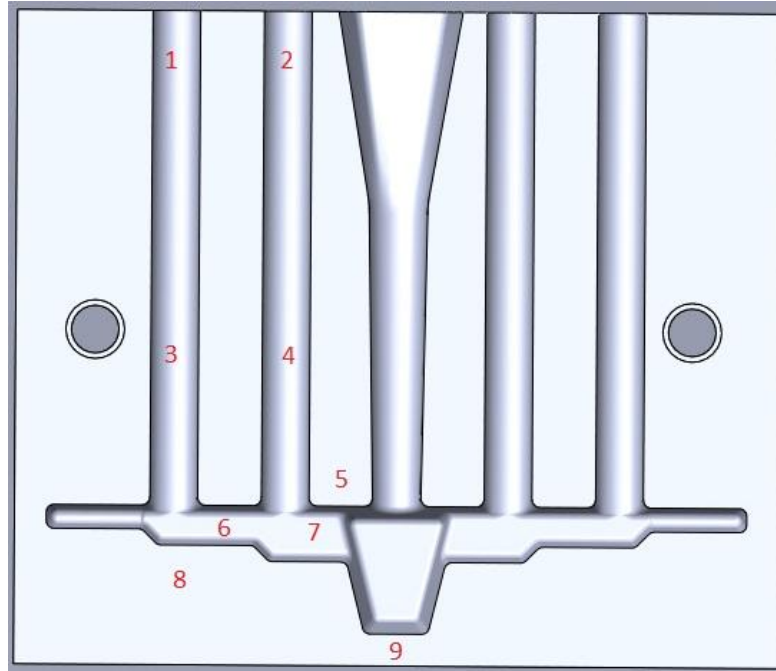


Figure 3.4: Thermocouple positions in the cylinder mold for measuring mold and melt temperatures during casting. The cylinders are 0.75 in (19mm) diameter and 7.5 in (109.5 mm) long.

Once the tensile bars were removed from the rest of the casting, they were heat treated using one of the two optimized heat treatments. For bars containing no Sc, this was a three hour heat treatment in air at 150 °C. For bars containing Sc, this heat treatment was an isochronal aging to 350 °C in air, using a 150 °C starting point, 50 °C increments and 3 hour hold times for each temperature. After being heat treated, they were machined following the ASTM B557 standard of 0.625 in (16 mm) diameter grips, and 0.5" (12.5 mm) diameter, 2 in (50 mm) long gage section. The tensile bars were then pulled at a strain rate of 10^{-4} /s using an extensometer to measure strain.

Table 3.5 shows the pouring temperatures used for the various alloys. Alloys 1-4 were poured in one heat, and alloys 5-8 were poured in a second heat. For alloys where multiple pours were done, the pour number is indicated after the pouring temperature.

Table 3.5
Pouring temperatures and number of pours of alloys cast in the cylinder bar mold

Alloy	Heat	# of molds poured	Pouring Temperature (C)
1	1	1	760
2	1	1	760
3	1	1	760
4	1	5	810 (1), 760 (2), 710 (3), <710 (4,5)
5	2	1	760
6	2	1	760
7	2	1	760
8	2	4	900 (1), 800 (2), 740 (3), 690 (4)

In the first heat, the Al ingot was melted, and degassing was performed. 99.9% pure Ytterbium was added to the melt, and the temperature was increased to 900 °C. The first alloy was then poured after the temperature fell to the target pouring temperature of 760 °C. This temperature was selected because a 100 °C superheat is common for casting processes, and the dilute Al-Sc(-Zr)(-Yb) alloys have melting points within a few degrees of pure Al at 660 °C (4). After pouring, more Yb was added, the temperature was increased, then allowed to cool to pouring temp when another casting was poured. This process was repeated until alloy 4 was reached. At this point, the amount of material remaining in the furnace was insufficient to allow for further heating after another pour. Because of this, the temperature was increased, and then allowed to fall as five more heats were poured. The first three pouring temperatures were measured, but the melt had cooled too much after the third pour to allow for measuring the last two pours due to concerns of the melt solidifying in the furnace.

The second heat was performed in much the same manner as the first, with degassing after the ingot was melted, followed by alloying additions, heating, cooling to pouring temperature, and more alloying additions. For the final alloy of the second heat, the maximum temperature was raised to allow for more time to pour and avoid solidification in the furnace. The material remaining was sufficient for four pours.

4. Results and Discussion

4.1 Cast Samples

Upon tensile testing the ASTM B-108 bars, both homogenized then aged and aged only showed strengths that were significantly lower than values that were expected based on other data for Al-Sc alloys. The remaining as-cast bars were subjected to x-ray Computed Tomography (CT) scans, and it was found that a large amount of shrinkage porosity existed in the lower grips, sometimes extending up into the gage section of the tensile bars. Also, a significant amount of microporosity was present, likely caused in part due to the fact that these heats were not degassed.

An undergraduate analyzed the mold in an attempt to determine the optimum casting conditions for aluminum alloys. Undergraduate students also attempted to find any areas where defects were likely to form. A CAD model of the mold was analyzed using MAGMASOFT version 5.0 solidification software, where pouring an AlSi05 alloy was simulated. AlSi05 is an Al alloy containing only 0.5 wt % Si. This alloy closely resembles the actual alloy used due to its low alloying content, eutectic equilibrium, and the alloy lies in the α -Al region of the Al-Si phase diagram, all of which are also characteristics of the Al-Sc alloys used. The simulation agreed with the experimental results that a pouring temperature of about 800 °C, and a mold preheat of about 400 °C was required to completely fill the mold. The model also predicted porosity of the same shape and size as was seen in the CT data, Figures 4.1 and 4.2 show the predicted and observed porosity data respectively. The mold CAD file was then modified to attempt to produce better castings, and simulated after each modification. Various techniques were attempted, including changing the diameter of the riser cylinders, altering the gating, and removing the filter block. None of the attempted modifications were able to produce sound castings.

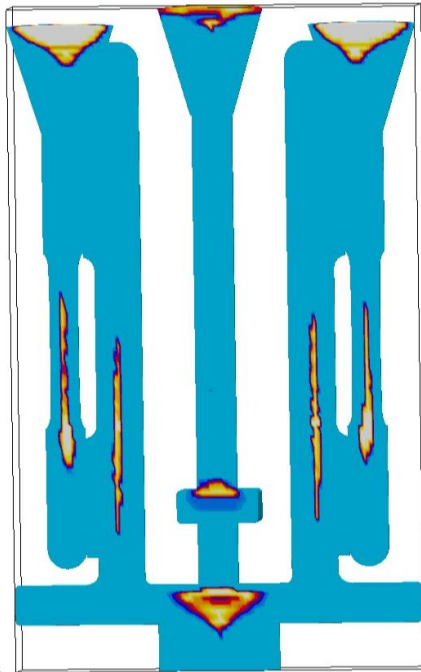


Figure 4.1: Predicted porosity in the tensile bar mold when cast at 800 °C and at a mold preheat of 400 °C using an Al-0.5Si alloy. Solid casting is light blue, porosity is red, orange, yellow and white in increasing order of severity.

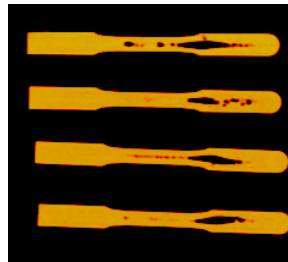


Figure 4.2: Observed porosity in tensile bars cast in the ASTM B-108 mold. Observe the large amount of porosity in the lower grip extending into the gage section, which agrees well with the simulation above.

The ASTM B-108 tensile bars exhibited a very wide range of properties due to the porosity and hot tearing defects. Failure strains varied from 14.4 to 30.4 % and yield strength varied from 69.5 to 113.1 MPa (10.1 to 16.4 ksi). On the fracture surfaces of the tensile bars, many pores were evident, indicating that there was a high amount of porosity present, most likely a result of the lack of degassing. This porosity seems to be a more important factor in determining failure than the shrinkage macroporosity that was observed in the CT scans, because none of the bars failed where the shrinkage macroporosity was located.

Some of the tensile bars that were pulled fractured outside of the gage section, at the radius between the gage section and the upper grip. Upon further examination, there were small cracks evident in this area on many of the as cast tensile bars. Figure 4.3 shows an example of one of these cracks on a tensile bar that has been heat treated but not pulled. It was determined that due to the geometry of the sample, the cracks were occurring as a result of hot tearing as the bar attempted to shrink as it cooled. The bar was not able to shrink due to being constrained at both ends, so hot tearing occurred. This shrinkage is a problem because at temperatures just below the melting point of the alloy, the strength of the thin casting skin is low, so any stress that is placed on the part is likely to cause surface cracks.



Figure 4.3: The red circle shows a small crack near the upper grip of a tensile bar that has been heat treated but not pulled. The crack is a result of hot tearing in the mold.

As a result of the unreliable data that was produced from the flawed ASTM B-108 mold, it was determined that a new mold strategy should be employed. In order to avoid the hot tearing problem, the mold was modified to cast cylinders rather than tensile bars.

The new cylinder mold (Figure 4.4) was also simulated in MAGMASOFT version 5.0 as an extension of the original undergraduate project, and optimized until it could be filled with the AlSi05 alloy at a 760 °C pouring temperature, with the mold at room temperature, to ensure easy filling in the foundry. Simulations showed that the mold should not produce any porosity in the center section of the cylinders where the gage section of the tensile bar would be located, but that one could expect a shrinkage cone at the top of the cylinders, and possibly some centerline porosity at the bottom of the cylinders, but not more than 25-50 mm (1-2 in) up the bar (Figure 4.5), leaving plenty of space for machining of a solid tensile bar. Further simulations with a mold preheat of 100 °C and 200 °C showed similar results to a room temperature mold, with no significant changes in the amount of porosity present in the casting.

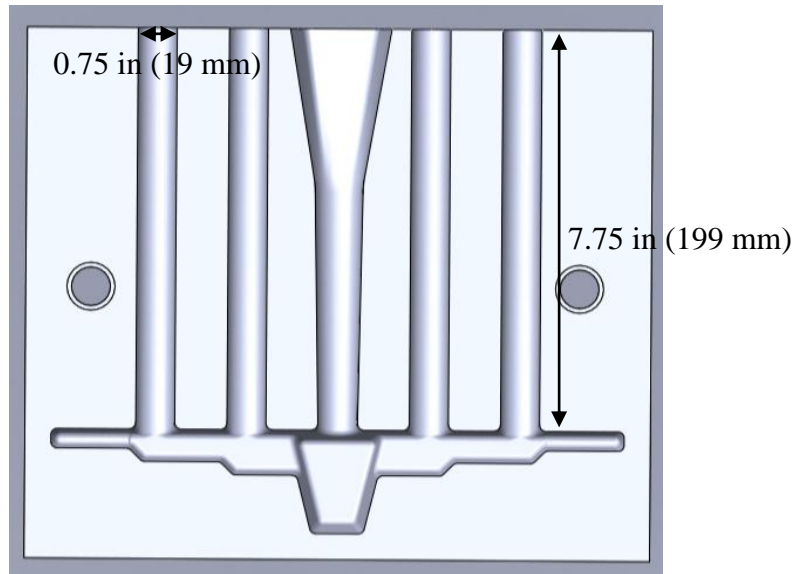


Figure 4.4: The new mold design, with the sprue in the center, creates 4 cylinders per casting which can be machined into tensile bars. The bar diameter is slightly larger than the finished grip diameter of 0.625 in (16 mm).

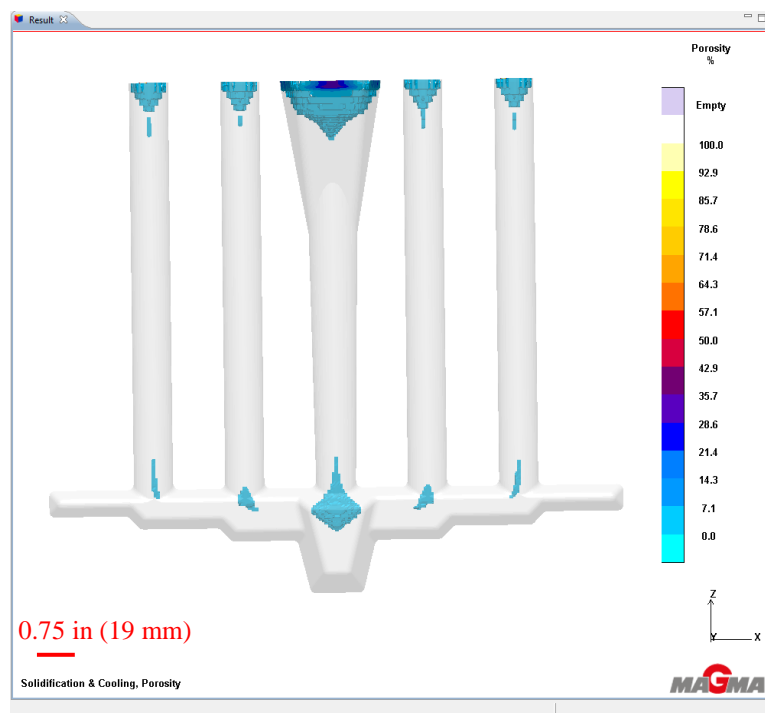


Figure 4.5: MAGMASoft simulation of the new mold at room temperature being filled with 760 °C AlSi05 showing porosity at the bottoms of the cylinders and typical cone shrinkage porosity at the top of the cylinders and in the pouring basin.

The thermocouples initially used in the mold had too slow of a response time to measure the cooling rate in the casting because they were large, and metal sheathed. In order to

get reliable data during the critical moments surrounding solidification, bare wire thermocouples were threaded through alumina sleeves, and inserted into the mold in place of the larger metal sheathed thermocouples. These were used for one pour, namely the third composition of the second heat, or alloy 7. The undergraduate group then modeled the mold with thermocouples in the same positions in MAGMASoft to verify the experimental results. Initially, their simulations showed the model cooling off faster than the experiment cooled. The actual mold was coated with a boron-nitride spray coating that worked as a mold release compound, and also acted as an insulator to slow heat transfer. Due to this coating, the heat transfer coefficient for the aluminum-mold interface was lowered in the software to half of its initial value so the experimental results more closely matched the modeled results. Figures 4.6 and 4.7 show the results of the experiment and the simulation. Thermocouples 3 and 5 (Figure 3.4) did not read correctly during the experiment so they are omitted from the figures below.

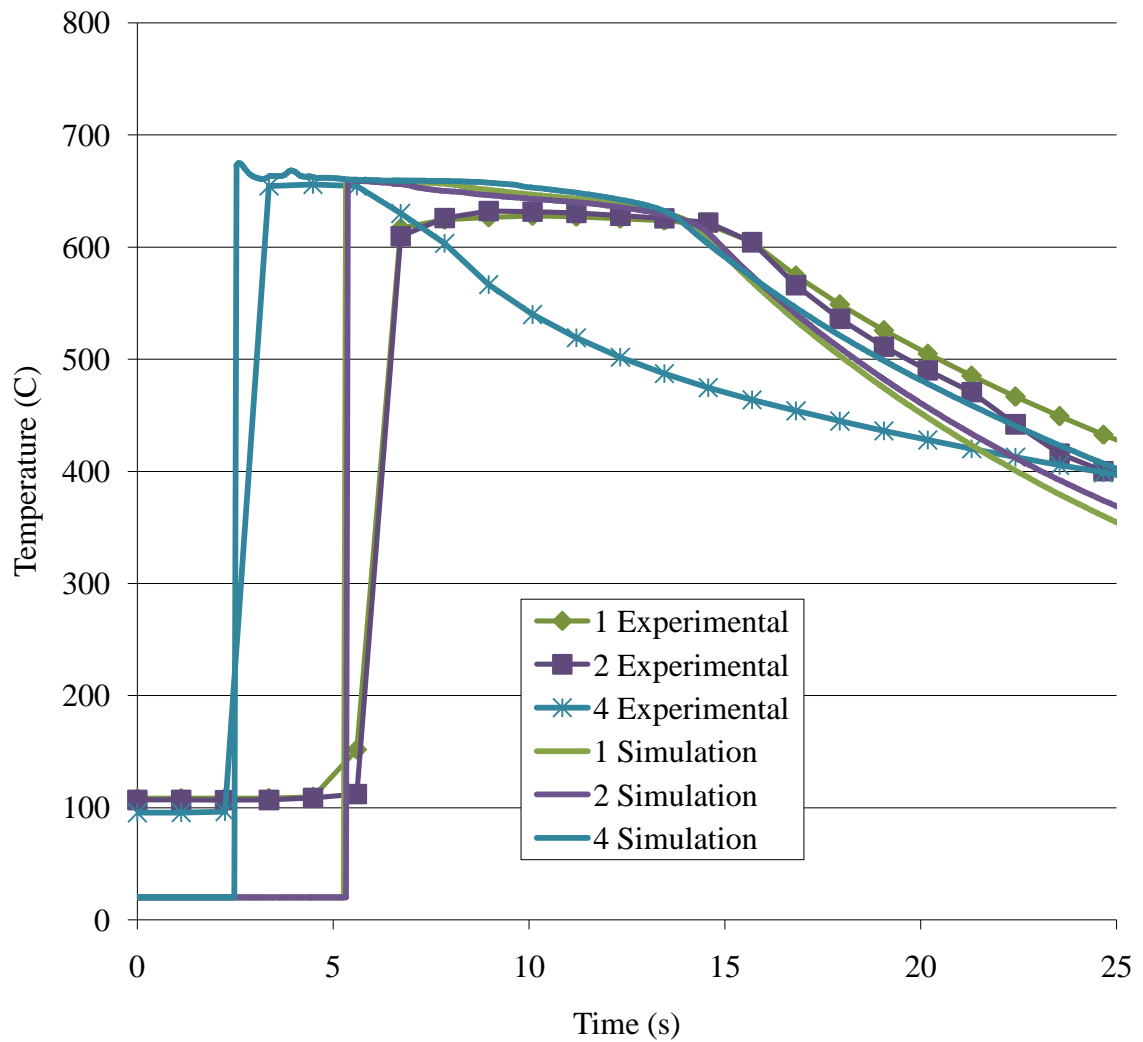


Figure 4.6: Experimental and simulated temperatures of thermocouples 1, 2 and 4 during a pour in the cylinder bar mold. Lines with the same color represent thermocouples in the same positions, where the lines with symbols are the experimental results.

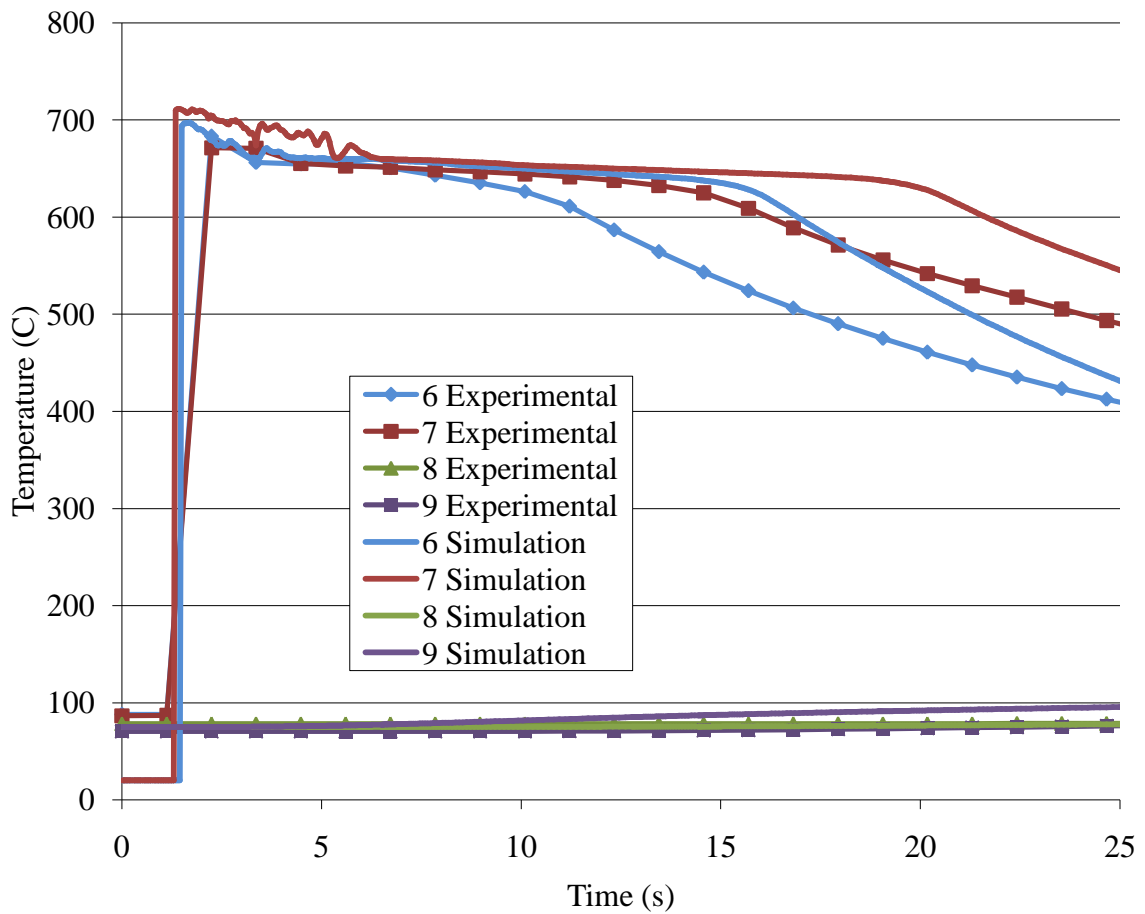


Figure 4.7: Experimental and simulated temperatures in the cylinder mold for thermocouples 6-9 during casting. Thermocouples 8 and 9 were monitoring mold temperature. Lines with the same color represent thermocouples in the same positions, where the lines with symbols are the experimental results.

Thermocouples 1, 2, 8 and 9 agree very well between simulation and experiment. However, the simulation results for thermocouples 4, 6, and 7 disagree with the results obtained in the experiment. In all cases, the simulation takes longer to solidify than the experiment does. One thing to note is that once the simulation thermocouples finish solidifying, the slope of the temperature vs. time curve is the same between the simulation and the experiment. This would indicate that perhaps there was an error in the placement of the thermocouples in the casting. If the thermocouples were measured to be too far into the casting, then they would take longer to cool through solidification in the simulation, compared to thermocouples that were located closer to the outside of the casting, which should cool more quickly.

Of the thermocouples that were exposed to the liquid metal in the mold for this experiment, only three reported temperatures above 655 °C, probably as a result of the relatively infrequent measurement rate of 1 Hz, the non-instantaneous response of the thermocouples during heating, in addition to the metal cooling as it flowed through the

mold. The thermocouples which read above 655 °C were 4, 6, and 7. Thermocouples 6 and 7 are located in the runners, and so they do not provide an accurate assessment of the temperatures in the cylinders. Thermocouple 4 was near the bottom of one of the cylinders, and over a span of three seconds, it dropped from a reading of 655 °C, which is approximately the melting point of our alloy, to 603 °C, giving an initial cooling rate of about 17 °C/s.

After casting in the cylinder bar mold several times, it was observed that this mold also exhibited a hot tearing problem at the top of the cylinders if the mold was overfilled. If too much metal was poured into the mold, the tops of the cylinders mushroomed out over the hole, creating the scenario where the bars are constrained at both ends, which lead to fracture as the metal shrank. The tops of the bars fractured about an inch into the mold as a result. By attempting to only just fill the mold instead of possibly overfilling it, this problem was eliminated.

4.2 Crucible-Melt Interaction Study

In the case of the zirconia and the graphite crucible, there was no discernable bonding between the master alloy and the crucible, as the master alloy was free to move in the crucible, and could be shaken out of the crucible. The magnesia crucible showed weak bonding to the master alloy. As the crucible was being sectioned the master alloy fell out due to the mechanical forces put on it during the cutting process. The bonding exhibited in the alumina crucible was sufficient that the master alloy could not be removed. This bonding did not seem to have any correlation to Sc losses to the crucible, as can be seen in the WDS results in Figure 4.8.

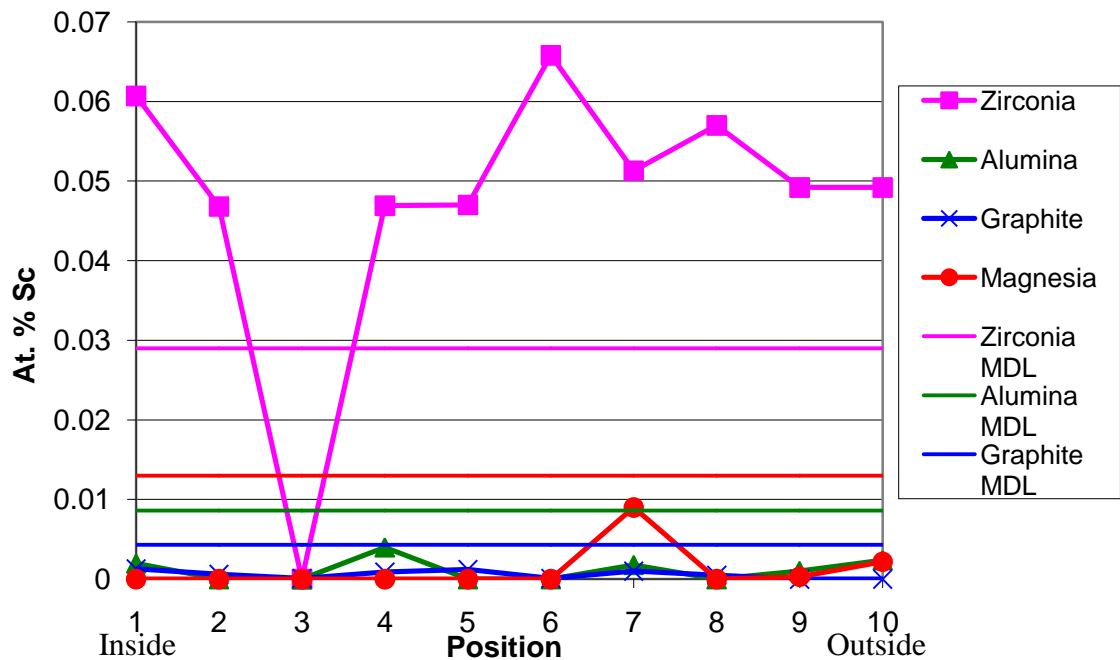


Figure 4.8: Scandium concentrations at points along WDS line scans where point 1 represents the inside edge of the crucible, and point 10 being nearest the outside edge. For simplicity, only the scans on the sides of a crucible are shown, but are representative of the scans across the bottom for the same crucible type. Solid horizontal lines represent the minimum detectable limit (MDL) of Sc for each crucible. The overall composition of the melt was 1.0 at. % Sc.

The minimum detectable limit of Sc as determined by the WDS software was different for each crucible. It varied from 0.0043 at. % for graphite to 0.029 at. % for zirconia. If there was diffusion of Sc into the crucible, it would be expected that an increase in the Sc content would be observed as one moved from the outside to the inside of the crucible. This is not evident in any of the WDS line scans. Additionally, the alumina, graphite, and magnesia crucibles reported statistically insignificant levels of Sc indicating no diffusion of Sc into the crucible was occurring, while the zirconia crucible had levels that were only double the MDL. It is possible that the elevated level of Sc observed in the

zirconia crucible would be found in a crucible that was not exposed to the Al-Sc master alloy simply as an impurity, because there is no overall trend to suggest that Sc is actually diffusing into the crucible, and the level found in the crucible is still two orders of magnitude lower than the level found in the master alloy.

No WDS measurements were taken of the master alloy because WDS requires homogeneity on a micron scale. Due to the slow cooling and supersaturation of the master alloy that was used, there were many large primary Al_3Sc precipitates present. Because of this high level of inhomogeneity, the composition of the master alloy could not be characterized using WDS.

All four crucible types used in this study showed convex menisci (Figure 4.9) indicating that the likelihood of a reaction between the melt and the crucible was small, due to the poor wetting behavior.

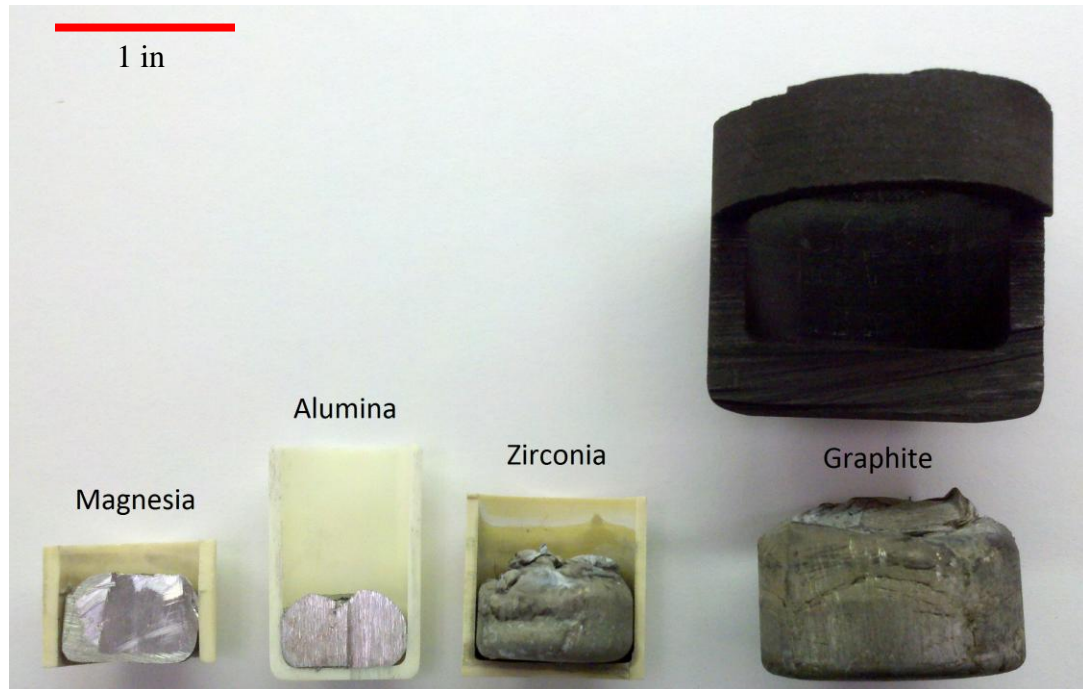


Figure 4.9: The four crucibles after solidification and sectioning showing convex menisci and a lack of wetting between the crucible and the melt.

The WDS data suggests that there is no loss of Sc occurring to the crucible, which is in direct conflict with the Gibbs free energy calculations which suggest that the reaction should occur spontaneously. This indicates that there must be some other factor that is preventing the reaction of Sc. One possible explanation is that a passivating layer of alumina could form on the interface between the melt and the crucible before the scandium has a chance to react with the crucibles. This layer could reduce the ability of Sc to react with the crucibles, because it must first diffuse through the alumina layer that has formed. As the master alloy starts to melt, the first liquid that forms will be relatively Sc poor, due to the first liquid that forms having the eutectic composition of only 0.28 at.

% Sc. During the time that the Sc poor liquid was exposed to the crucible, it is possible that the aluminum reduced the crucible and formed a passivating layer that prevented the Sc from reacting with the crucible.

It is also possible that the activity of Sc in the solution is too low for the reaction to occur spontaneously. This minimum value can be calculated by the relationship given in equation 4.1,

$$\Delta G_{RT} = -RT \ln \left(\frac{a_{product}}{a_{reactant}} \right), \quad \text{eq. 4.1}$$

and assuming that Sc is not in its standard state, but everything else is. If this is done, then equation 4.1 becomes equation 4.2,

$$\Delta G_{RT} = -RT \ln \left(\frac{1}{a_{Sc}^4} \right) \quad \text{eq. 4.2}$$

for the zirconia crucible, and equation 4.3,

$$\Delta G_{RT} = -RT \ln \left(\frac{1}{a_{Sc}^2} \right) \quad \text{eq. 4.3}$$

for the magnesia and alumina crucibles. Using the calculated Gibbs free energies and a temperature of 1173 K, the minimum values of the activity of Sc were determined to be 4×10^{-6} , 8×10^{-4} , and 7×10^{-6} for zirconia, magnesia, and alumina respectively for the reaction to take place. The activity of scandium was calculated to be 2.5×10^{-7} using the chemical potential of scandium in aluminum which was calculated to be equal to the Gibbs free energy of Al_3Sc at 1173K, or -1.483×10^5 J/mol, and then converting using the relationship shown in equation 4.4,

$$\mu_{Sc} = G_{Sc(l)}^0 + RT \ln(a_{Sc}) \quad \text{eq. 4.4}$$

where $G_{Sc(l)}^0$ was approximated to be zero, because its value would be very small in comparison to the value of μ_{Sc} at -148,254 J/mole of atoms at 1173K. The activity indicates that there should be no reaction, even though the scandium oxide is more thermodynamically stable than the other oxides.

4.3 Composition Determination

ICP was performed on each composition once, and on the final composition of each pour 3 times to assess any fade that might be occurring as the melt is left in the crucible for an extended time. Table 4.1 shows the results of the experimentation, where ND stands for Not Detected. Iron and Si impurity concentrations were found to be in the range of 0.003-0.012 at. %, and 0.006-0.015 at. % respectively. The 99.99 % purity master alloy used was certified as containing impurities listed in table 4.2. It is not immediately clear where the impurities are coming from, however the values are still acceptably low. Acceptable limits for especially pure alloys are 0.07 and 0.08 at. % for Fe and Si respectively (14). Contents of Fe higher than that limit will negatively impact the Al structure due to the formation of Fe based precipitates. Higher Si contents will react with the Al and Sc to form compounds that remove Sc from solution (14).

Table 4.1
Results of the ICP composition measurements in at. %

Pour #	Sc		Zr		Yb		Fe	Si
	Measured	Target	Measured	Target	Measured	Target	Measured	Measured
1	ND	0.000	ND	0.000	0.0074	0.010	0.0039	0.0063
2	ND	0.000	ND	0.000	0.0160	0.020	0.0036	0.0059
3	ND	0.000	0.0189	0.030	0.0165	0.020	0.0031	0.0061
4 (1)	0.0534	0.060	0.0174	0.030	0.0166	0.020	0.0061	0.0094
4 (3)	0.0513	0.060	0.0173	0.030	0.0166	0.020	0.0069	0.0109
4 (5)	0.0519	0.060	0.0160	0.030	0.0180	0.020	0.0073	0.0114
5	ND	0.000	0.0202	0.030	ND	0.000	0.0030	0.0063
6	0.0672	0.080	0.0205	0.030	ND	0.000	0.0050	0.0101
7	0.0867	0.110	0.0190	0.030	ND	0.000	0.0087	0.0099
8 (1)	0.1489	0.140	0.0234	0.030	ND	0.000	0.0122	0.0154
8 (2)	0.1501	0.140	0.0241	0.030	ND	0.000	0.0104	0.0171
8 (4)	0.1215	0.140	0.0206	0.030	ND	0.000	0.0139	0.0124

Table 4.2
Impurities present in the 99.99% Al master alloy

Element	Composition (at. %)
Copper	0.00138%
Iron	0.00105%
Silicon	0.00149%
Zinc	0.00006%

Table 4.3 shows the alloying yield for the additions of Sc, Zr, and Yb. The yield for Sc and Yb are both acceptable, but the yield on Zr is low. It is not immediately clear where the Zr is going, since it doesn't appear to be exhibiting fade, or reverse fade if it were segregating to the bottom of the melt. Sc also does not appear to fade over time, which is another encouraging sign that none is being lost to oxidation reactions or to reactions with the crucible as it is held.

Table 4.3
Yield of elements added to alloys

Element	Yield
Sc	78-100%
Zr	53-80%
Yb	74-90%

4.4 Heat Treatment Optimization

Figures 4.10 and 4.11 show the results of the heat treatment optimization for Yb containing alloys, where hardness and conductivity are plotted against aging temperature.

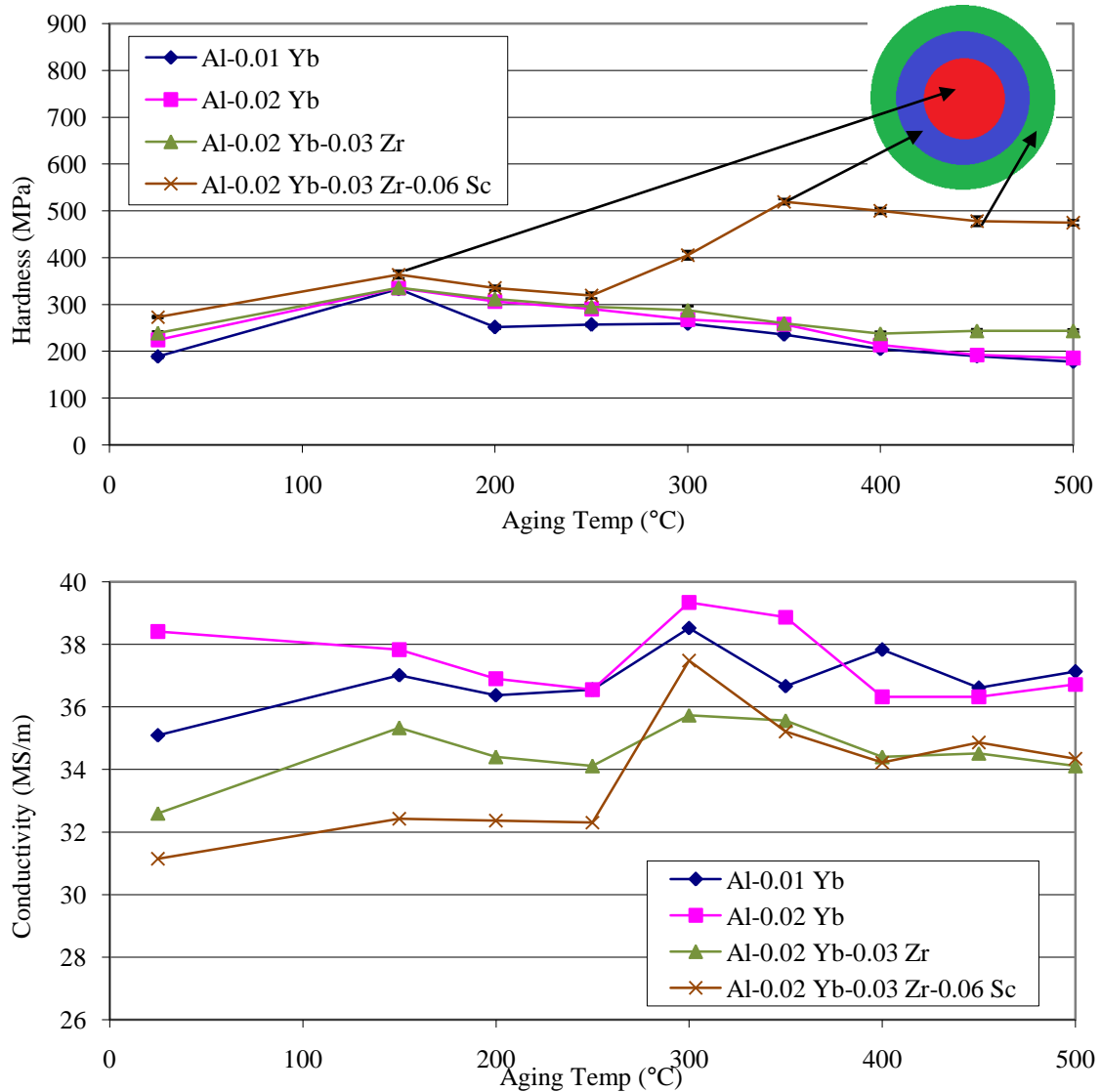


Figure 4.10 (top) and Figure 4.11 (bottom): Isochronal aging performed from 150 to 500 °C on samples of 4 different compositions. Non Sc containing samples clearly exhibit peak aging at 150 °C, where the Sc containing alloys exhibit peak aging at 350 °C. Conductivity increases as solute atoms precipitate out of solution, and eventually decreases again as precipitates break down to allow others to coarsen, increasing solute atoms in solution. The colored concentric circles are a representative sketch of the cored structure of the precipitates, where the red core can be correlated to the Yb precipitation peak, the blue shell to the Sc precipitation peak, and the green outer shell to the Zr precipitation.

The Al-0.02 Yb-0.03 Zr-0.06 Sc at. % alloy exhibits two hardness peaks, the first is due to the Al_3Yb precipitation reaction, and the second is due to the Al_3Sc precipitation. It is known that Yb diffuses through Al significantly faster than Sc or Zr which allows it to nucleate and grow at a much lower temperature compared to Sc or Zr, which is the cause

for this dual peak (14). Alloys with higher levels of Zr usually exhibit a peak around 450-500 °C due to the Zr precipitating out of solution and diffusing to the existing Al_3Sc precipitates (2,11). In these alloys, the level of Zr was not high enough to produce a high temperature peak, but it did help to prevent the onset of overaging for the Sc alloy. Typically in alloys that contain Sc without Zr, peak aging occurs between 300 and 350 °C, and the alloys have significantly overaged by 400 °C (2,11). The presence of Zr helps to stave off overaging for the Sc alloy, as even at 500 °C, the alloy maintains over 90 % of its peak hardness.

Figures 4.12 and 4.13 show the isochronal aging study that was performed on a series of Al-Zr and Al-Zr-Sc alloys.

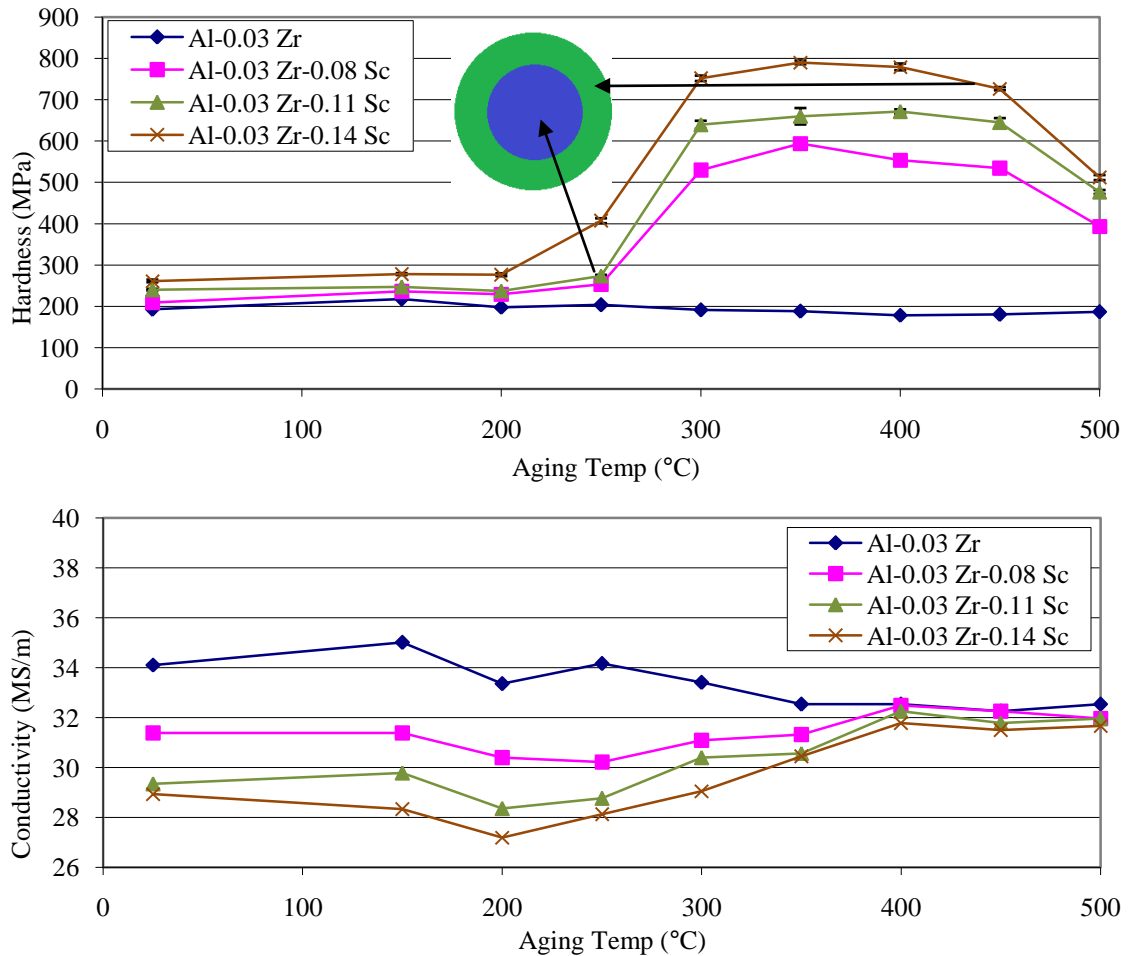


Figure 4.12 (top) and Figure 4.13 (bottom): Isochronal aging performed from 150 °C to 500 °C on samples of 4 different compositions. Al-0.03Zr at. % exhibits a weak peak at 150 °C, while the Sc containing alloys all exhibit peak aging at 350 °C. Conductivity increases when solute atoms precipitate out of solution around 200 °C, and eventually decreases again as precipitates break down to allow others to coarsen, increasing solute atoms in solution. The colored concentric circles are a representative sketch of the cored structure of the precipitates, where the the blue core corresponds to the Sc precipitation peak, and the green outer shell to the Zr precipitation.

Again the level of Zr in the alloys is too low to produce a secondary higher temperature peak from Zr precipitation; however the sustained overaging resistance is again present, as hardness is maintained to 450 °C after which significant overaging begins. The peak hardness exhibited by the Al-0.03Zr-0.08Sc at. % alloy of 594 ± 6 MPa is 74 MPa higher than the peak strength achieved by the Al-0.02Yb-0.03Zr-0.06Sc at. % of 520 ± 6 MPa.

This would seem to indicate that simply replacing Sc with Yb on a per atom basis will not result in an alloy with the same hardness levels as an Yb free alloy. Tensile results will be used to confirm a difference in strength between the two alloys.

The grain size measurements that were taken on alloys 5-8 show a trend of decreasing grain size with increasing Sc content. All four samples exhibited columnar grains oriented radially in the sample (Figure 4.14), however the average size of these grains decreased from sample 5 to sample 8 (Table 4.4). While the average grain size did decrease, none of the samples exhibited the fine, equiaxed grains that are typically seen in Al-Sc alloys where primary precipitates have refined the grain structure. In a study of an Al-0.10Sc-0.10Zr at. % alloy, a grain structure of $\sim 50\text{ }\mu\text{m}$ diameter equiaxed grains was reported, which is significantly smaller than the mm scale grains present in our samples (2). This would indicate that while total solute content of 0.20 at. % is enough for primary precipitation and grain refinement in the literature, the 0.17 at. % in the current study is not sufficient for grain refinement.



Figure 4.14: Samples after polishing and etching for grain size measurements. From left to right, alloy 5, 6, 7, and 8(1). The grains get smaller in size from left to right.

Table 4.4
Grain size of alloys 5-8 as cast

Alloy	Grain Size
5	$7.13\text{ mm}^2/\text{grain}$ ($0.0110\text{ in}^2/\text{grain}$)
6	$5.48\text{ mm}^2/\text{grain}$ ($0.00850\text{ in}^2/\text{grain}$)
7	$4.60\text{ mm}^2/\text{grain}$ ($0.00713\text{ in}^2/\text{grain}$)
8 (1)	$4.19\text{ mm}^2/\text{grain}$ ($0.00650\text{ in}^2/\text{grain}$)

4.5 Ultrasonic Measurements

Table 4.5 shows the results of the ultrasonic measurements of elastic modulus and Poisson's ratio, where the uncertainties reported are standard error calculated using the three velocity measurements to calculate three values for each material property. The alloys all exhibit an elastic modulus that is very close to that of pure Al at 70 GPa, which

is expected, because the alloys are 99.7+ % pure aluminum. The Poisson's ratios are also close to that of pure Al at 0.35. The shear modulus of pure aluminum is 26 GPa, and the values observed agree well with that number except for alloys 3 and 7, which are also out of agreement in terms of elastic modulus as well.

Table 4.5

Results of the ultrasonic measurement of elastic modulus and Poisson's ratio

Sample	Poisson's Ratio			E (GPa)			G (GPa)		
1	0.332	±	0.002	71.5	±	0.4	26.8	±	0.2
2	0.330	±	0.003	71.3	±	0.7	26.8	±	0.2
3	0.345	±	0.003	66.6	±	0.2	24.8	±	0.1
4 (1)	0.351	±	0.001	70.1	±	0.2	25.9	±	0.1
5	0.345	±	0.001	71.2	±	0.2	26.5	±	0.1
6	0.347	±	0.001	71.5	±	0.4	26.6	±	0.2
7	0.340	±	0.001	73.7	±	0.4	27.5	±	0.2
8 (1)	0.308	±	0.032	68.2	±	2.0	26.1	±	0.6

Figure 4.15 is a main effects plot showing the effect of each alloying element on the elastic modulus. The plot was created by performing an ANOVA (ANalysis Of VAriance) on the elastic modulus to determine which factors (alloying elements) are significant in terms of having an impact on the elastic modulus to a 95% confidence level. Each element is significant, all with P values below 0.001 (Appendix A). These effects are significant because even though these alloys are nearly pure aluminum, the additions of these elements are having an effect on the material properties. This indicates the additions have very different properties in terms of modulus compared to pure aluminum. Based on the melting points of the precipitates, one would expect that the elastic modulus of Al-Yb, Al-Sc, and Al-Zr precipitates would be higher than that of pure aluminum, since the elastic modulus of a substance is proportional to its melting temperature. It is possible that the sample sizes used for this experimentation were too large, and so other effects are skewing the results, such as the presence of defects in the material or signal attenuation.

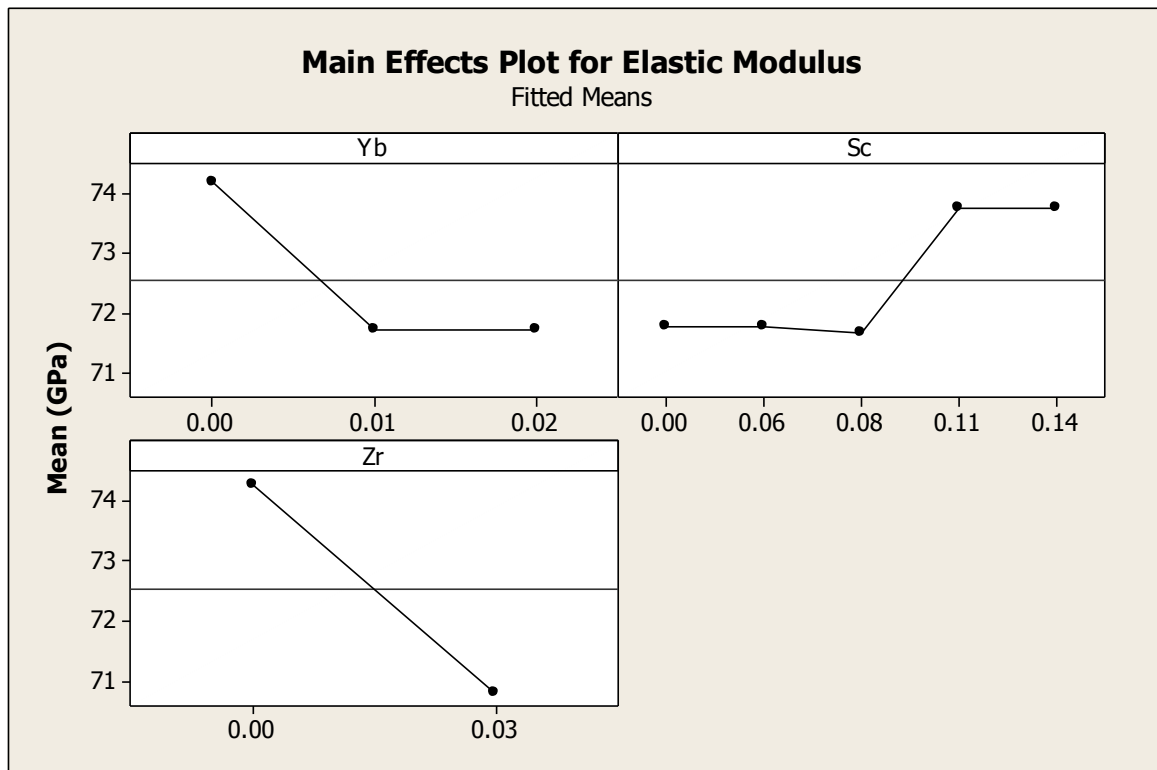


Figure 4.15: Main effects plot of alloying additions on the elastic modulus (in GPa).

4.6 Tensile Bars

Each pour of the cylinder mold created 4 cylinders, three of which were used for tensile testing. The fourth bar was used for the hardness and conductivity tests. After being removed from the gating, subjected to the optimized heat treatment, and machined to ASTM B557, the three tensile specimens were tested. Table 4.6 shows the results of the testing, where the uncertainty reported is the standard error. Alloys 4 and 8 which were poured more than once are noted with a number in parenthesis that indicates the pour order.

Table 4.6
Results of tensile testing alloys 1-8

Alloy (pour#)	Composition	Stress at Offset Yield (MPa)	Peak Stress (MPa)	Strain at Break (mm/mm)
1	Al-0.01Yb	26 ± 2	45 ± 8	0.3 ± 0.1
2	Al-0.02Yb	33.6 ± 0.8	63.2 ± 0.3	0.50 ± 0.02
3	Al-0.02Yb-0.03Zr	32.6 ± 0.8	61.8 ± 0.5	0.54 ± 0.03
4 (1)	Al-0.02Yb-0.03Zr-0.06Sc	106 ± 2	141.9 ± 0.9	0.29 ± 0.01
4 (2)	Al-0.02Yb-0.03Zr-0.06Sc	111.5 ± 0.4	143.5 ± 0.2	0.35 ± 0.01
4 (3)	Al-0.02Yb-0.03Zr-0.06Sc	111 ± 1	144 ± 2	0.26 ± 0.04
4 (4)	Al-0.02Yb-0.03Zr-0.06Sc	109 ± 1	140 ± 6	0.20 ± 0.05
4 (5)	Al-0.02Yb-0.03Zr-0.06Sc	106 ± 2	138 ± 4	0.15 ± 0.03
5	Al-0.03Zr	24.2 ± 0.4	51.4 ± 0.2	0.63 ± 0.02
6	Al-0.03Zr-0.08Sc	131.5 ± 0.3	159.8 ± 0.5	0.196 ± 0.005
7	Al-0.03Zr-0.11Sc	163 ± 1	193.7 ± 0.5	0.19 ± 0.01
8 (1)	Al-0.03Zr-0.14Sc	198 ± 1	222 ± 1	0.15 ± 0.02
8 (2)	Al-0.03Zr-0.14Sc	178 ± 6	211 ± 5	0.2 ± 0.01
8 (3)	Al-0.03Zr-0.14Sc	194 ± 5	228 ± 1	0.2 ± 0.007
8 (4)	Al-0.03Zr-0.14Sc	199 ± 3	234.2 ± 0.7	0.23 ± 0.01

From cursory examination of the table, it can be seen that alloys that contain scandium have significantly higher strength values, and lower strain values than those alloys that do not contain scandium. Also, one can see that alloy 4 which should compare to alloy 6 seems to have lower strength and higher ductility. These effects are examined using general linear models to test the effect of each alloying addition on the yield stress, peak stress, and strain at break values. Also a two sample t-test is used to determine if the differences in observed yield and peak stresses, as well as strain at break are a result of statistically different means. Appendix A lists the relevant statistical data for each calculation.

Figures 4.16 through 4.18 show the effect of alloying additions for all the various alloys on the tensile properties of the alloys. Figure 4.16 is a main effects plot of yield strength as a function of alloying additions. It can be seen that Zr has no effect on yield strength, however as expected Sc has a very strong effect on yield strength. Yb is barely significant for yield strength with a p value of 0.029. From examination of the hardness study, these trends make sense. Alloys with Sc are significantly stronger than alloys without. Also, alloys with Sc exhibit a large hardness peak. The alloys that contain Yb also exhibit an aging peak, but the peak is not as large as the Sc peak. No peaks are seen that can be attributed to Zr, and so it makes sense that Zr is not significant on the yield strength.

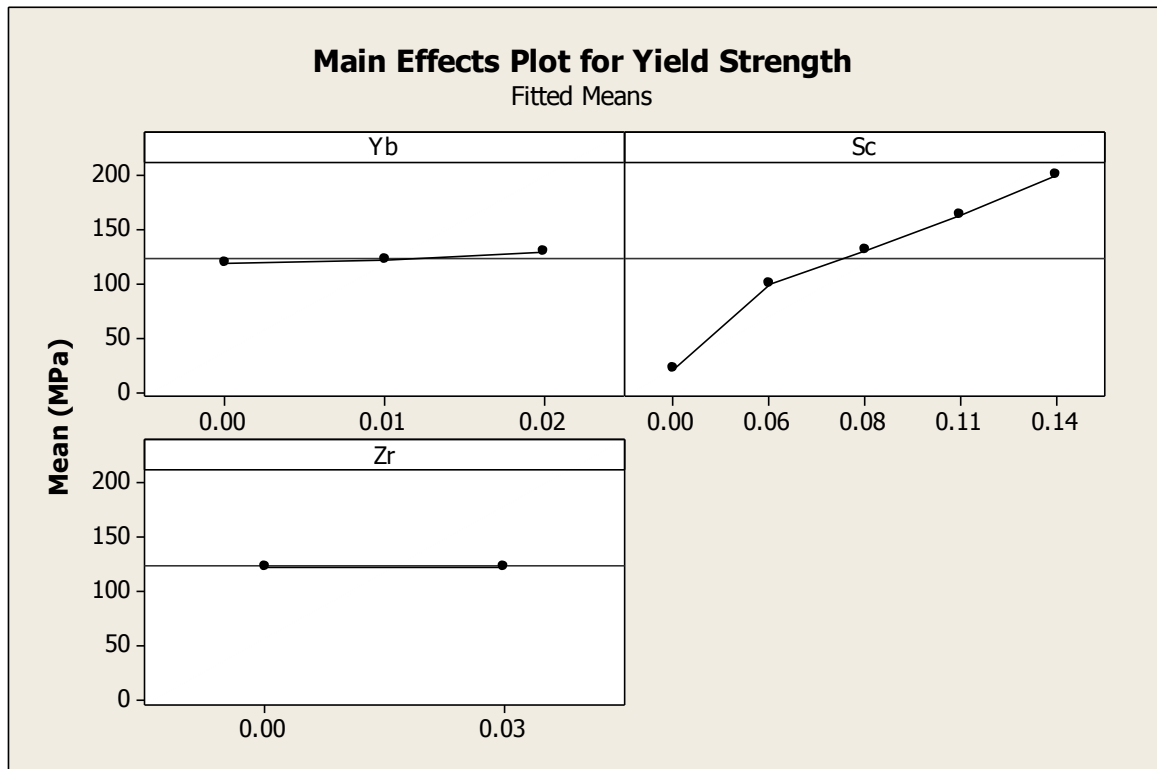


Figure 4.16: Main effects plot of alloying additions on yield strength.

Figure 4.17 shows the relationship between the alloying additions and the ultimate tensile strength (UTS). Again, Sc and Yb are significant, with Sc having a much stronger effect on the UTS compared to Yb. Zr is not significant for UTS. These results also make sense for the same reasons that the yield strength effects make sense.

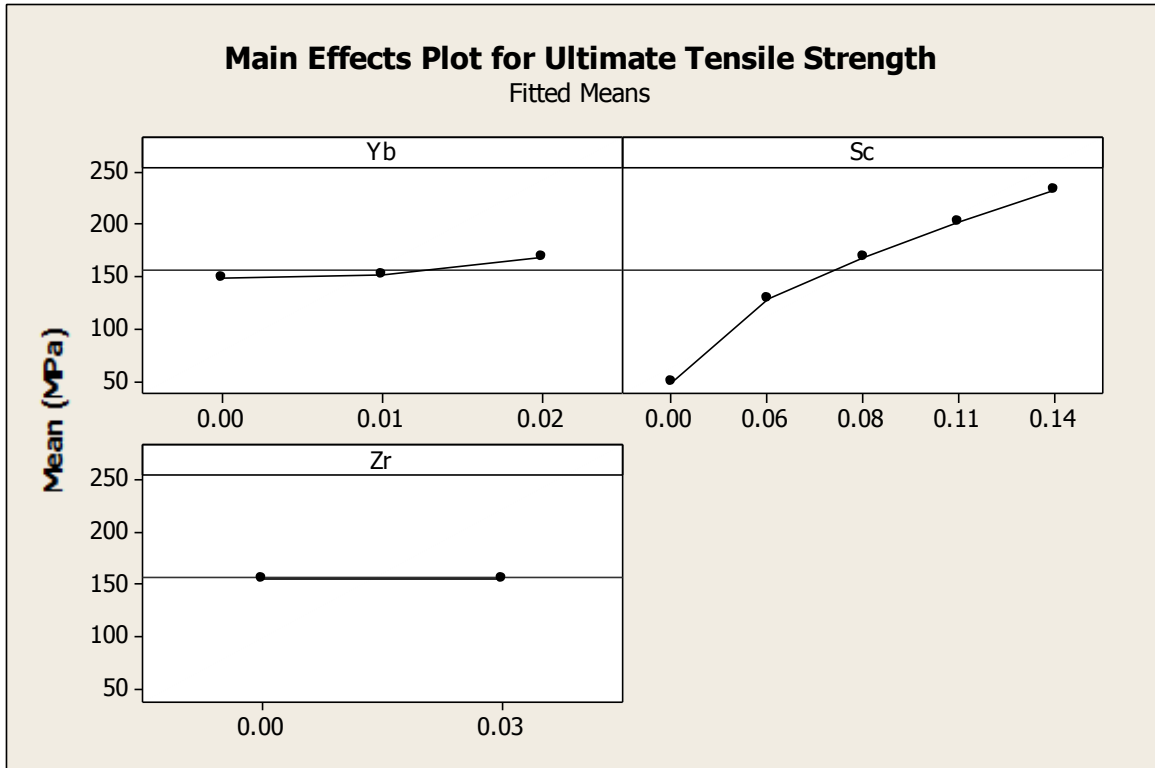


Figure 4.17: Main effects plot of alloying additions on UTS.

Figure 4.18 shows the relationship between the alloying additions and the elongation observed. Again Yb and Sc are significant, and again Zr is not. These results are interesting, because adding additional Yb causes an increase in the elongation. In general, alloys that are stronger are usually not more ductile. The most interesting thing is that Sc seems to have only a weak effect on the ductility of the alloys, which is odd because of the very strong effect it has on the strength. It is possible that this effect is driven by defects or porosity, which are more prevalent in the bars that were poured at lower temperatures. Looking at the bars containing scandium and ignoring the bars poured at lower temperatures, the trend seems to be that increasing Sc content decreases ductility as would be expected. The plot for the effect of Sc on the mean exhibits a large dip at 0.06 at. %. This indicates that for some reason the mean elongation in the 0.06 at. % Sc samples was low, possibly because most of the elongation effect is attributed to the presence of Yb in those alloys.

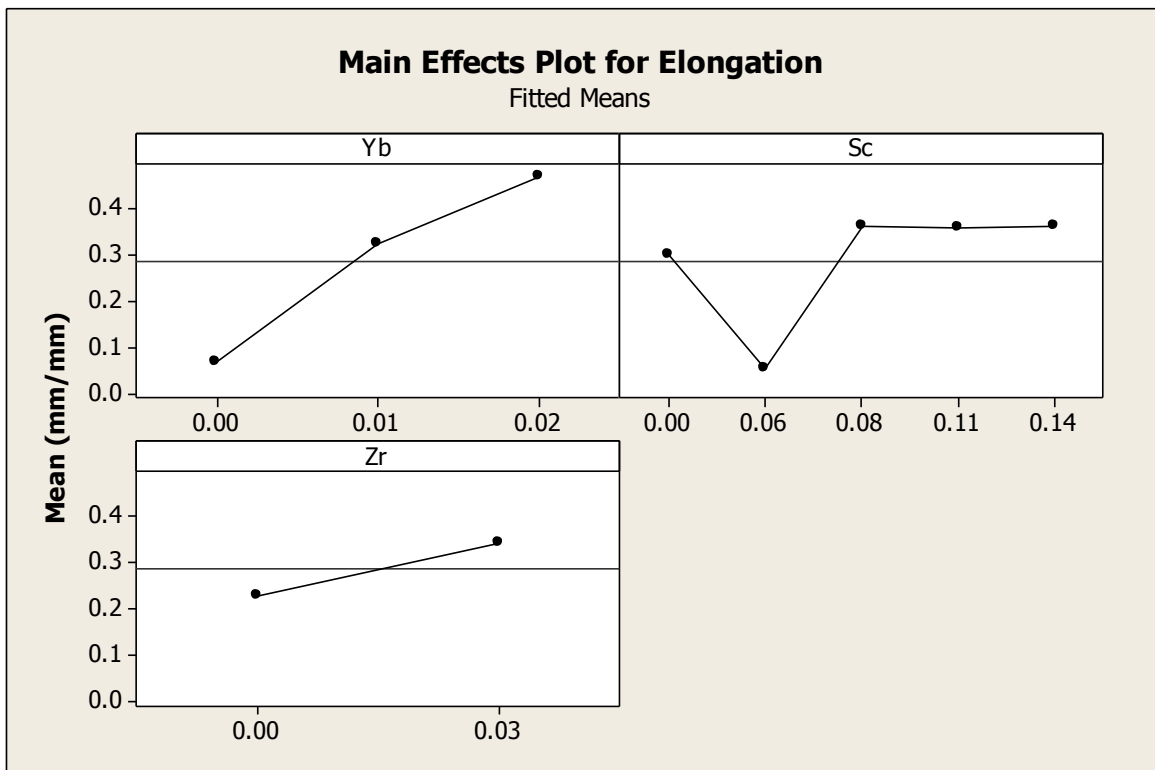


Figure 4.18: Main effects plot of alloying additions on elongation.

Alloys with scandium exhibit significantly higher strength values, and significantly lower strain values as would be expected because ductility and strength typically have an inverse relationship. Alloys with higher scandium contents are stronger than those with lower scandium contents, which would also be expected, due to the higher volume fraction of precipitates present in alloys with more scandium. Using the lever rule and assuming negligible scandium solubility in α -Al at the aging temperature, one can roughly estimate the volume fraction of precipitates present by taking the total amount of solute present (0.11 at. % for alloys 4 and 6), and multiplying by 4, because the solute atoms make up one fourth of the atoms in a precipitate with the Al_3Sc structure. This

estimate is reasonable because isochronal aging allows for nucleation of precipitates at the lowest possible temperature, insuring essentially zero solubility for solute atoms (11). Also, the lattice parameter of Al_3Sc is 0.4103 nm, and for pure Al, it is 0.40496 nm, a mismatch of 1.3% (2). The addition of Zr serves to decrease this mismatch, with the lattice parameter of $\text{Al}_3(\text{Sc}_{1-x}\text{Zr}_x)$ varying from 0.4103 nm at $x=0$ to 0.4092 at $x=0.5$ (2).

An attempt was made to measure the size of the precipitates in these alloys using a field emission scanning electron microscope. The instrument was not able to resolve the precipitates, so the size of the precipitates in these alloys was not measured in this study; however they have been assessed in many previous studies. Table 4.7 shows a summary of these other precipitate radius studies. Many studies reported significant coarsening above 350 °C for Al-Sc-Zr alloys for durations of 10 or more hours(2). From this information, one can conclude that the amount of solute has little effect on diameter of the precipitates when compared to the duration and temperature of aging. For our system of alloys, it is reasonable to assume that the alloys had precipitates of ~2.5 nm radius, due to the isochronal heat treatment that the samples underwent. At precipitate radii of 2-3 nm or larger, the dominant mechanism for strengthening has been found to be Orowan dislocation looping for these alloy systems (2). Smaller precipitates are sheared by the dislocations, but as the precipitates become larger, it is easier for the dislocations to loop around them as a bypass mechanism, rather than shear them.

Table 4.7
The precipitate radii found for various alloys and heat treatments

Alloy (at. %)	Aging Treatment	R (nm)
Al-0.06Sc-0.06Zr (11)	Isochronal to 350 °C	~2
Al-0.12Sc (11)	300 °C creep test	3
Al-0.07Sc-0.02Zr (11)	300 °C creep test	2.3
Al-0.10Sc-0.10Zr (2)	Isochronal to 350 °C	~2
Al-0.09Sc-0.02Zr (2)	475 °C 15 hr	9.6
Al-0.09Sc-0.03Zr (2)	450 °C 32 hr	16
Al-0.09Sc-0.05Zr (2)	Isothermal to 300 °C	~2
Al-0.03Yb (14)	Isochronal to 300 °C	3.8
Al-0.03Yb (14)	Isochronal to 300 °C + 3 hr 300 °C	4.4
Al-0.03Yb (14)	Isochronal to 300 °C + 64 hr 300 °C	9.7
Al-0.06Sc-0.02Zr-0.02Yb (14)	3 hr 300 °C	~2
Al-0.06Sc-0.02Zr-0.02Yb (14)	96 hr 300 °C	~2.5
Al-0.06Sc-0.02Zr-0.02Yb (14)	1536 hr 300 °C	~3
Al-0.06Sc-0.02Yb (14)	24 hr 300 °C	2.9
Al-0.06Sc-0.02Yb (14)	1536 hr 300 °C	5.5

The Orowan strengthening can be calculated with equation 1.1, knowing that for pure Al, $M=3.06$, $G_{Al}=25.4$ GPa, $\nu=0.345$ for Al, $b=0.286$ nm, $\bar{R} = 1.96$ nm (if $R=2.5$ nm), and using equation 4.5.

$$\lambda_{e-e} = \left(\sqrt{\frac{2\pi}{3\phi}} - \frac{\pi}{2} \right) \langle 2.5 \rangle \quad \text{eq. 4.5 (2)}$$

Table 4.8 shows the predicted Orowan strengthening from the various alloys, and the increases observed in the tensile bars in terms of hardness and UTS for the same alloys.

Table 4.8

Expected Orowan strengthening values in MPa for 2.5, and 4 nm radius particles for each Sc containing alloy, and observed hardness and UTS increases for the same alloys

Alloy	ϕ (%)	$\Delta\sigma_{or}$ 2.5 nm	$\Delta\sigma_{or}$ 4.0 nm	Hardness Increase (MPa)	UTS Increase (MPa)
Al-0.02Yb-0.03Zr-0.06Sc	0.44	180.9	133.5	246	93
Al-0.03Zr-0.08Sc	0.44	180.9	133.5	386	108
Al-0.03Zr-0.11Sc	0.56	206.1	152.2	430	142
Al-0.03Zr-0.14Sc	0.64	229.2	169.2	529	172

The expected strengthening effect from the two alloys used for comparison is higher than observed. . The hardness increase is calculated by subtracting the hardness at peak aging from the as-cast hardness. The UTS values are calculated by taking the average UTS value for each alloy, and then subtracting the UTS exhibited by the Al-0.03Zr alloy, because that alloy most closely represents pure Al of the the alloys used in this study. The Zr alloy exhibits a very small strength increase from the as-cast state, and its hardness at peak aging is comparable to the starting hardness values of the other alloys here, so it is a sensible estimate to use that as a baseline value of the UTS for these alloys. The expected Orowan strengthening values line up best with a material that has precipitates of radius 4nm. The estimate of 2.5 nm was based on other heat treatment studies done on similar alloys, but based off of the Orowan calculations, perhaps an estimate of 4.0 nm is more accurate.

Figures 4.19-4.21 examine the differences in terms of strength and elongation between the Al-0.02Yb-0.03Zr-0.06Sc at. % alloy (alloy 4) and the Al-0.03Zr-0.08Sc at. % alloys (alloy 6). Figure 4.19 is a boxplot of the yield strength of alloys 4 and 6 for comparison. It can be seen that the yield strengths of the two alloys are different, so clearly substitution of Yb for Sc does not result in the same yield strength. The larger spread in the data for alloy 4 is likely because alloy 4 was poured 5 times, at 5 different superheats, where alloy 6 was only poured once, and consists of 3 samples, compared to 13 for alloy 4.

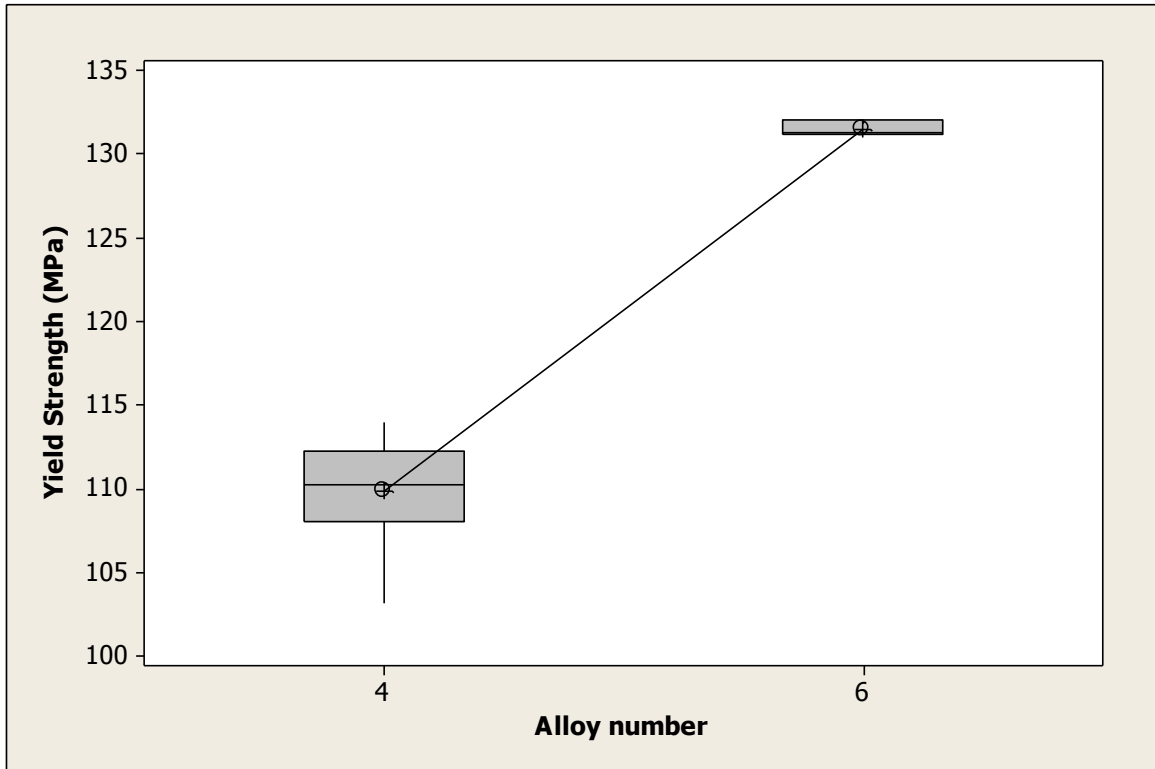


Figure 4.19: Boxplot of the yield strength of alloys 4 and 6.

Figure 4.20 shows the UTS of alloys 4 and 6 also differ, meaning that Yb substitution for Sc also does not produce an alloy with the same UTS. Again, alloy 4 is comprised of more samples than alloy 6, so the larger spread in the data for alloy 4 can probably be attributed to that.

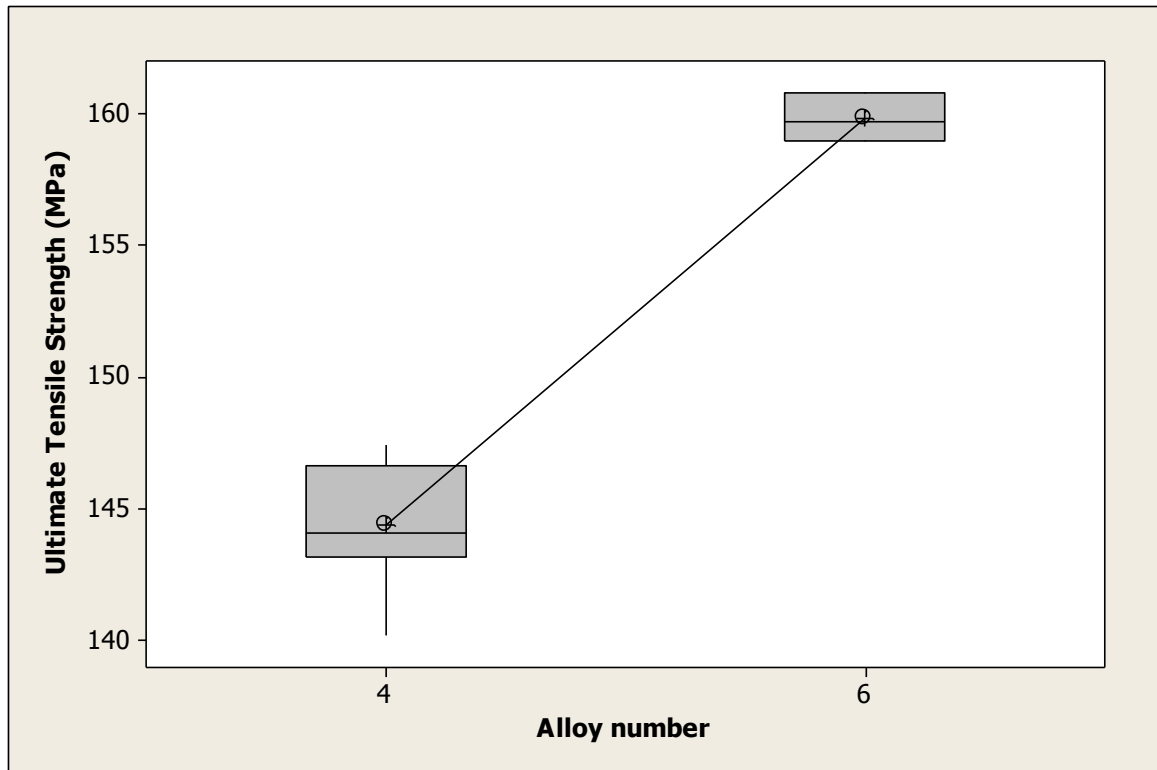


Figure 4.20: Boxplot of the UTS of alloys 4 and 6.

Figure 4.21 shows the relationship between elongation at failure and the two alloys. It can be seen that elongation is different between the two alloys, with the Yb alloy exhibiting more elongation, but the Yb alloy also exhibits more variation in the data. Alloy 4 again shows larger variation in comparison to alloy 6.

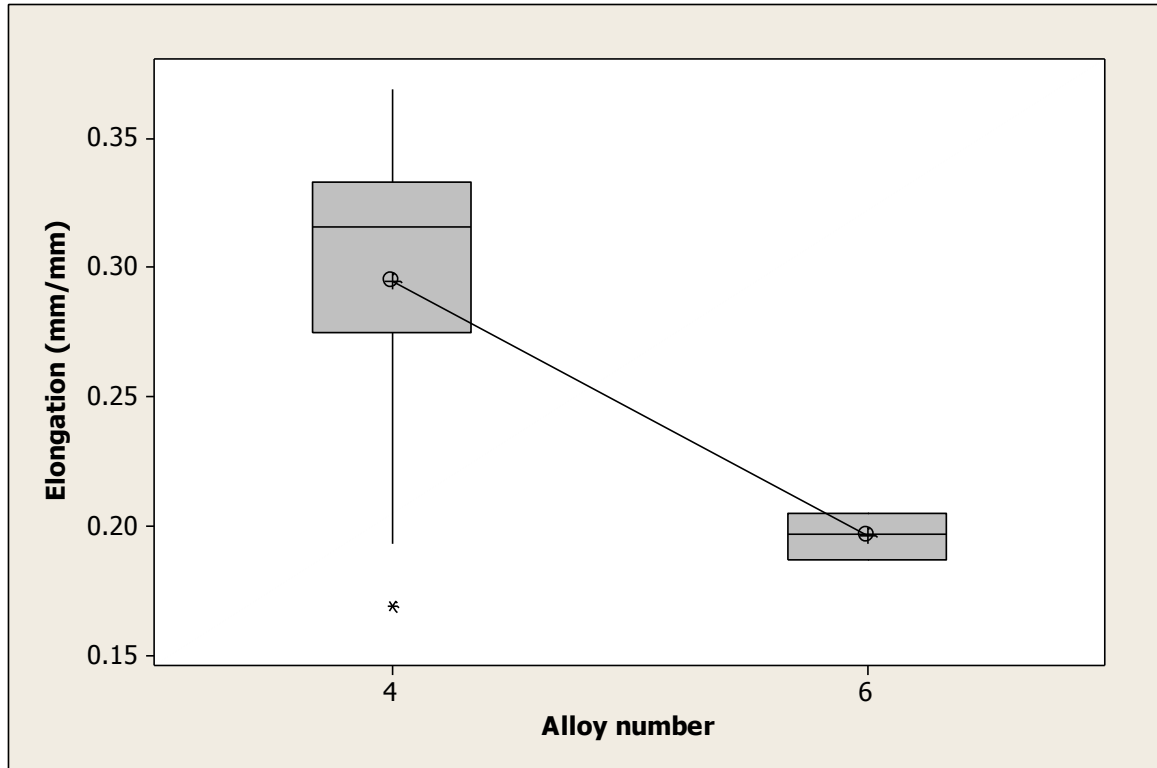


Figure 4.21: Boxplot of the elongation values exhibited by alloys 4 and 6

These plots indicate that the strength and elongation values of these two alloys are definitely different. Using a simple minded approach knowing that Yb will sit on the Sc site in Al_3Sc precipitates, and because it is substituted at a 1:1 atomic ratio, that the strength should be the same between the two alloys, because the overall precipitate volume fraction should remain constant. The strength does not remain the same, so there must be some explanation for this difference. One possible explanation is that the Al_3Yb precipitates which form first in the Yb containing alloys coarsen significantly before the Sc precipitates out and joins the Al_3Yb . If this were to happen, then the Al_3Yb precipitates would be reduced in number, which would cause a corresponding increase in the average inter-particle spacing. This would result in a decrease in the overall strength of the alloy. When a high enough temperature is reached for Sc precipitation to begin, the Sc would most likely preferentially precipitate to existing precipitates rather than form new precipitates, as has been shown with Zr diffusing to existing Al_3Sc precipitates.

This theory can be supported by examining the diffusion distances of Yb, Sc, and Zr in Al after 3 hours at 300 °C. A rough estimate of the diffusion distance for comparative purposes can be calculated using equation 4.6

$$L = 2\sqrt{Dt} \quad \text{eq. 4.6 (17)}$$

where L is the diffusion length, D is the diffusion coefficient, and t is time.

The diffusion coefficient can be calculated using equation 4.7

$$D = D_0 e^{\left(\frac{-Q_d}{RT}\right)} \quad \text{eq. 4.7 (17)}$$

where D_0 is the pre-exponential factor, Q_d is the activation energy for diffusion, R is the gas constant, and T is the temperature in K.

The approximate diffusion lengths and the diffusion coefficients for Yb, Sc, and Zr are listed in Table 4.9

Table 4.9
Diffusion lengths and coefficients for Yb, Sc, and Zr after 3 hours at 300 °C

Element	L (m)	D (m ² /s)
Yb	1.6×10^{-6}	5.7×10^{-17} (14)
Sc	6.2×10^{-8}	9.0×10^{-20} (1)
Zr	5.2×10^{-10}	6.3×10^{-24} (1)

Using equation 4.2, we approximate the average edge to edge inter particle spacing to be between 50 and 80 nm as the average radius varies from 2.5 to 4.0 nm. We can see that at these heat treatment conditions, Yb should diffuse approximately 1600 nm, compared to 62 nm for Sc and 0.52 nm for Zr. This indicates that Yb has the ability to diffuse roughly 25 times farther than Sc at these conditions. It is therefore possible that by the time the Sc is coming out of solution and precipitating to the existing Al_3Yb precipitates, the precipitates have coarsened significantly due to the much higher diffusion rate of Yb in Al. Also, the extremely low value for Zr indicates that it should not be significantly precipitating at this temperature, which is what is observed.

The tensile bars fractured in one of two distinct manners. Some of the specimens fractured in a typical cone-cup type fracture, and exhibited a large amount of necking, with some samples reducing to less than half of their starting diameters, or a reduction in area of over 75%. Other samples failed in a 45 degree type plane fracture. Figure 4.21 shows the various types of failures seen. Some bars did not actually fail completely, because the tensile tests were set to stop when stress dropped below 10% of peak stress. Other bars actually fractured completely. In general, bars that exhibited the highest elongation at failure were bars that exhibited a large amount of necking, and had cone-cup fracture surfaces. Table 4.11 shows the fracture behavior for the samples. Bars that had lower elongation typically had 45 degree plane type fracture surfaces, and large defects present on the fracture surface. Bars from alloy 4(4) and 4(5) failed with the 45

degree plane type failure, and on large defects present in the bars which appeared to be oxidized pieces of metal, roughly 1-2mm in size. This was probably a result of the extremely low pouring temperature used for these alloys. As the lower pouring temperatures allows for many defects to form in the casting, such as increased entrapment of gasses that are not able to escape due to the shorter solidification time in alloys poured at a lower temperature.

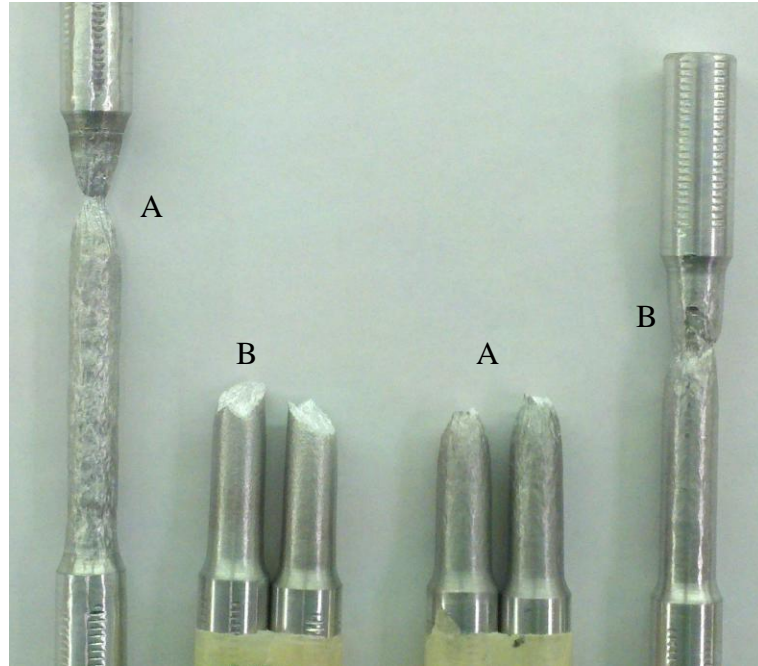


Figure 4.22: Tensile bars exhibiting the four failure modes. Tensile bars were from alloys 5, 8, 4, and 6 from left to right. *A* indicates a cone-cup type fracture, and *B* indicates a 45 degree plane type fracture. The bars on the outside did not fracture entirely, the two on the inside fractured completely.

Table 4.9
Fracture surface geometry of the tensile samples

Alloys	45 Degree Plane	Cone-Cup
1 - 4 (3)		x
4 (4), 4 (5)	x	
5 - 8 (3)		x
8 (4)	x	

Unless the bars failed on some large defect present in the gage section, they failed by the expected cone-cup mechanism. The cone-cup mechanism is expected, because in a bar with a circular cross section, the preferred 45 degree failure plane that is perpendicular to the surface, as calculated using Mohr's circle, results in infinite 45 degree failure planes which intersect to form a cone. The bars that did not fail by the cone-cup mechanism

must have necessarily failed on some large defect that did not allow the bars to reach a state where significant necking occurred.

5. Future Work

This work has focused on evaluating the ambient temperature properties of heat treated Al-Sc-Zr-Yb alloys, but has not examined the high temperature properties. Further work on this topic could examine the effect of elevated temperatures on the mechanical properties of these alloys. This information would be valuable if these alloys were to be employed in any sort of commercial application where high temperature retention of strength is important.

This work also did not measure the radius of the precipitates in the alloys. A TEM study of these alloys to explore precipitate size and distribution would be a useful addition to this data. TEM data could confirm the hypothesis that the low strength observed in the Yb alloys is due to coarsening of the Yb precipitates due to the heat treatment procedure.

Further research on these alloys could also explore different heat treatment strategies to avoid loss of strength in the Yb alloys. An aging procedure which creates the Yb precipitates, and then skips to a higher temperature at which Sc precipitates begin to form could help avoid the coarsening of the Yb precipitates at the intermediate temperatures between Yb precipitate formation and Sc precipitate formation.

6. Conclusions

The first hypothesis was that Sc would be lost to common crucible types during melting, as suggested by the Gibbs free energy calculations.

Through the crucible-melt interaction study, it was shown that in our system, the main element of concern, Sc was not lost to four common crucible types during a worst case scenario of very high melt temperature, and long hold times, and so the hypothesis was determined to be false.

The thermodynamic study of these systems suggests that there is a driving force to create a scandium oxide at the crucible-melt interface; however the activity of Sc is too low for the scandium oxide to be produced. It is also possible that an oxide coating of alumina could form early in the melting process when the melt is relatively poor in Sc and create a barrier for Sc when the melt finally reaches the point where all of the Sc is in solution.

The second hypothesis was that Yb could be substituted for some Sc in an Al-Sc-Zr alloy to maintain the strength while decreasing the cost, because Yb will substitute for Sc in Al_3Sc precipitates yielding comparable strength.

This was found to be false. In an alloy where 0.02 at. % Sc was replaced with Yb, the peak strength, and the offset yield strength decreased, and the ductility increased, by 22 MPa, 15 MPa, and 0.1 mm/mm respectively while the alloys were subjected to the same heat treatment.

The best tensile properties were seen in alloys that were poured at a temperature of at least 760 °C. Temperatures below this value resulted in significantly increased defects present in the bars. Many of the bars that were poured below this temperature failed on defects of 1-5 mm in size that were present in the bars, and as a result, did not reach peak strength or elongation values exhibited by the other bars.

It was determined that an induction furnace is suitable for the melting of these alloys, as the induction effects strongly promote mixing of the melt, leading to complete dissolution of primary precipitates found in the master alloys used.

7. References

1. Knipling KE, Dunand DC, Seidman DN. Criteria for developing castable, creep-resistant aluminum-based alloys – A review. *Zeitschrift fur Metallkunde*. 2006;97(3):246-265
2. Knipling KE, Karnesky RA, Lee CP, Dunand DC, Seidman DN. Precipitation evolution in Al-0.1Sc, Al-0.1Zr and Al-0.1Sc-0.1Zr (at%) alloys during isochronal aging. *Acta Materialia*. 2010;58:5184-5195
3. Murray JL. Al-Sc Phase Diagram, ASM Alloy Phase Diagrams Center, P. Villars, editor-in-chief; H. Okamoto and K. Cenzual, section editors; <http://www1.asminternational.org/AsmEnterprise/APD>, ASM International, Materials Park (OH), 2010.
4. Toropova LS, Eskin DG, Kharakterova ML, Dobatkina TV. *Advanced Aluminum Alloys Containing Scandium*. 1st. Milton Park, Abingdon, Oxon: Taylor & Francis; 1998.
5. Meyers MA. *Dynamic Behavior of Materials*. 1st. New York(NY): John Wiley & Sons, Inc.; 1994.
6. Babic E, Zlatic V. Changes of the lattice parameter in Al 3d alloys due to the virtual bound state. *Solid State Communications*. 1976;18(6):705-708
7. A worldwide supplier of rare earth, non-ferrous, advanced ceramic materials! – Stanford Materials [Internet]. Aliso Viejo (CA): Stanford Materials. Scandium (Sc); [cited 2011 Aug 4]; Available from: <http://www.stanfordmaterials.com/sc.html>
8. Kuang JP, Harding RA, Campbell J. Investigation into refractories as crucible and mould materials for melting and casting γ -TiAl alloys. *Materials Science and Technology*. September 2000;16(9):1007-1016
9. Sadrenzhaad SK, Raz SB. Interaction between Refractory Crucible Materials and the Melted NiTi Shape-Memory Alloy. *Metallurgical and Materials Science Transactions B*. June 2005;36B:395-403
10. Drits MY, Ber LB, Bykov YG, Toropova LS, Anastasyeva GK. Ageing of alloy Al-0.3 at% Sc. *Physics of Metals and Metallography*. 1984;57(6):118-126

11. Knipling KE, Seidman DN, Dunand DC. Ambient- and high-temperature mechanical properties of isochronally aged Al-0.06Sc, Al-0.06Zr and Al-0.06Sc-0.06Zr (at.%) alloys. *Acta Materialia*. 2011;59:943-954
12. Okamoto H. Al-Zr Phase Diagram, ASM Alloy Phase Diagrams Center, P. Villars, editor-in-chief; H. Okamoto and K. Cenzual, section editors; <http://www1.asminternational.org/AsmEnterprise/APD>, ASM International, Materials Park (OH), 2010.
13. A worldwide supplier of rare earth, non-ferrous, advanced ceramic materials! – Stanford Materials [Internet]. Aliso Viejo (CA): Stanford Materials. Ytterbium (Yb); [cited 2011 Aug 4]; Available from: <http://www.stanfordmaterials.com/yb.html>
14. van Dalen M. Microstructure and Creep Properties of Al-Sc Alloys Micro-alloyed with Lanthanides (Yb or Gd) and Transition Metals (Ti or Zr) [PhD Dissertation]. Evanston (IL): Northwestern University; 2007. 289p.
15. Olympus - Non Destructive Ultrasonic Test Equipment, Innov-X, High Speed Video, Microscopes, NDT, Remote Visual Inspection, Ultrasonic, Phased Array, Eddy Current, Thickness Gages, Flaw Detectors [Internet]. Olympus Corporation. Elastic Modulus Measurement; 2011 [cited 2011 Aug 17]. Available from: <http://www.olympus-ims.com/en/applications/elastic-modulus-measurement/>
16. Zakharov VV, Rostova TD. Effect of Scandium, Transition Metals, and Admixtures on Strengthening of Aluminum Alloys due to Decomposition of the Solid Solution. *Metal Science and Heat Treatment*. 2007;49(9,10):435-442
17. Callister WD. *Fundamentals of Materials Science and Engineering*. 2nd ed. Hoboken (NJ): John Wiley & Sons, Inc.; 2005. 712 p.

8. Appendix A

Minitab output for general linear models and two sample t-tests of the effects of composition on elastic modulus, yield strength, ultimate tensile strength, and elongation. When assuming a confidence interval of 95%, P values that are below 0.05 are considered significant.

General Linear Model: E versus Yb, Sc, Zr

Factor	Type	Levels	Values
Yb	fixed	3	0.00, 0.01, 0.02
Sc	fixed	5	0.00, 0.06, 0.08, 0.11, 0.14
Zr	fixed	2	0.00, 0.03

Analysis of Variance for E, using Adjusted SS for Tests

Source	DF	Seq SS	Adj SS	Adj MS	F	P
Yb	2	28.9364	9.1347	4.5674	12.21	0.001
Sc	4	18.3491	12.3104	3.0776	8.23	0.001
Zr	1	18.1162	18.1162	18.1162	48.45	0.000
Error	16	5.9828	5.9828	0.3739		
Total	23	71.3845				

S = 0.611494 R-Sq = 91.62% R-Sq(adj) = 87.95%

General Linear Model: Yield Strength versus Yb, Sc, Zr

Factor	Type	Levels	Values
Yb	fixed	3	0.00, 0.01, 0.02
Sc	fixed	5	0.00, 0.06, 0.08, 0.11, 0.14
Zr	fixed	2	0.00, 0.03

Analysis of Variance for Yield Strength, using Adjusted SS for Tests

Source	DF	Seq SS	Adj SS	Adj MS	F	P
Yb	2	71704	273	137	3.88	0.029
Sc	4	98411	87089	21772	617.97	0.000
Zr	1	2	2	2	0.05	0.831
Error	41	1445	1445	35		
Total	48	171561				

S = 5.93568 R-Sq = 99.16% R-Sq(adj) = 99.01%

Unusual Observations for Yield Strength

	Yield				
Obs	Strength	Fit	SE Fit	Residual	St Resid
41	169.353	192.157	1.713	-22.804	-4.01 R
43	176.414	192.157	1.713	-15.743	-2.77 R

R denotes an observation with a large standardized residual.

General Linear Model: UTS versus Yb, Sc, Zr

Factor	Type	Levels	Values
Yb	fixed	3	0.00, 0.01, 0.02
Sc	fixed	5	0.00, 0.06, 0.08, 0.11, 0.14
Zr	fixed	2	0.00, 0.03

Analysis of Variance for UTS, using Adjusted SS for Tests

Source	DF	Seq SS	Adj SS	Adj MS	F	P
Yb	2	74928	1135	567	7.61	0.002
Sc	4	111530	99204	24801	332.49	0.000
Zr	1	1	1	1	0.01	0.933
Error	41	3058	3058	75		
Total	48	189517				

S = 8.63668 R-Sq = 98.39% R-Sq(adj) = 98.11%

Unusual Observations for UTS

Obs	UTS	Fit	SE Fit	Residual	St Resid
1	28.800	44.867	4.986	-16.067	-2.28 R
23	123.000	141.647	1.981	-18.647	-2.22 R
27	123.000	141.647	1.981	-18.647	-2.22 R
30	19.300	40.667	4.986	-21.367	-3.03 R
41	202.300	223.825	2.493	-21.525	-2.60 R

R denotes an observation with a large standardized residual.

General Linear Model: Elongation versus Yb, Sc, Zr

Factor	Type	Levels	Values
Yb	fixed	3	0.00, 0.01, 0.02
Sc	fixed	5	0.00, 0.06, 0.08, 0.11, 0.14
Zr	fixed	2	0.00, 0.03

Analysis of Variance for Elongation, using Adjusted SS for Tests

Source	DF	Seq SS	Adj SS	Adj MS	F	P
Yb	2	0.280099	0.277899	0.138950	25.06	0.000
Sc	4	0.156211	0.155850	0.038962	7.03	0.000
Zr	1	0.018816	0.018816	0.018816	3.39	0.074
Error	35	0.194030	0.194030	0.005544		
Total	42	0.649156				

S = 0.0744562 R-Sq = 70.11% R-Sq(adj) = 64.13%

Unusual Observations for Elongation

Obs	Elongation	Fit	SE Fit	Residual	St Resid
1	0.067000	0.281333	0.042987	-0.214333	-3.53 R
2	0.496000	0.281333	0.042987	0.214667	3.53 R
5	0.292000	0.428000	0.042987	-0.136000	-2.24 R

R denotes an observation with a large standardized residual.

Two-Sample T-Test and CI: Yield Strength, Sample2

Two-sample T for Yield Strength

Sample2	N	Mean	StDev	SE Mean
4	13	109.82	2.91	0.81
6	3	131.509	0.466	0.27

Difference = μ (4) - μ (6)
Estimate for difference: -21.691
95% CI for difference: (-23.527, -19.855)
T-Test of difference = 0 (vs not =): T-Value = -25.52 P-Value = 0.000 DF = 13

Two-Sample T-Test and CI: UTS, Sample2

Two-sample T for UTS

Sample2	N	Mean	StDev	SE Mean
4	13	144.38	2.12	0.59
6	3	159.833	0.907	0.52

Difference = μ (4) - μ (6)
Estimate for difference: -15.449
95% CI for difference: (-17.264, -13.633)
T-Test of difference = 0 (vs not =): T-Value = -19.62 P-Value = 0.000 DF = 8

Two-Sample T-Test and CI: Elongation, Sample2

Two-sample T for Elongation

Sample2	N	Mean	StDev	SE Mean
4	13	0.2949	0.0577	0.016
6	3	0.19633	0.00902	0.0052

Difference = μ (4) - μ (6)
Estimate for difference: 0.0986
95% CI for difference: (0.0623, 0.1349)
T-Test of difference = 0 (vs not =): T-Value = 5.86 P-Value = 0.000 DF = 13

9. Appendix B

Right to republish copyrighted images.

COPYRIGHT PERMISSION REQUEST

TO: ASM International Permissions Sue Sellers Product & Project Administrator ASM International 9639 Kinsman Road Materials Park, Ohio 44073-0002 USA Phone: +440 338-5151 ext 5465 FAX: +440 338-4634 Email: Permissions@asminternational.org	FROM: Complete all contact information Your name: Nicholas Johnson Title: Graduate Student Affiliation: Michigan Technological University Address: 1400 Townsend Drive Houghton, Michigan 49931-1295 Phone: 651-497-7769 FAX: Email: ndjohnso@mtu.edu
---	--

I am preparing an article/chapter for publication in the following formats (*check as applicable*):

☐ Print only
☐ Internet only
☒ Print & electronic media

The information will be used for (*check as applicable*):

☐ Journal article
☐ Internal company records
☐ Student Course Material
☐ Conference presentation
☒ Dissertation
☐ Commercial Publication*

The article/chapter title will be: Introduction

The publication title will be: Processing and mechanical properties of cast aluminum containing scandium, zirconium, and ytterbium

The publisher is: ProQuest/UMI

Planned year of publication: 2011

Book print run: 6

I hereby request permission for non-exclusive world rights in the above publication and all subsequent editions, revisions, and derivative works in English and foreign translations, in the formats indicated above for print or any electronic (CD/web) media, from the following copyrighted content by ASM International:

Okamoto H. Al-Zr Phase Diagram, ASM Alloy Phase Diagrams Center, P. Villars, editor-in-chief; H. Okamoto and K. Cenzual, section editors; <http://www1.asmiinternational.org/AsmEnterprise/APD>, ASM International, Materials Park (OH), 2010.

Murray J.L. Al-Sc Phase Diagram, ASM Alloy Phase Diagrams Center, P. Villars, editor-in-chief; H. Okamoto and K. Cenzual, section editors; <http://www1.asmiinternational.org/AsmEnterprise/APD>, ASM International, Materials Park (OH), 2010.

Please sign this release form:

Signed:

Date: 9/21/11

I (we) grant permission requested above. Please ensure credit as publisher by citing the above ASM publication as a reference, and by including the ASM International logo. All rights reserved. www.asmiinternational.org

Signed: ASM Intern

Date:

9/23/2011

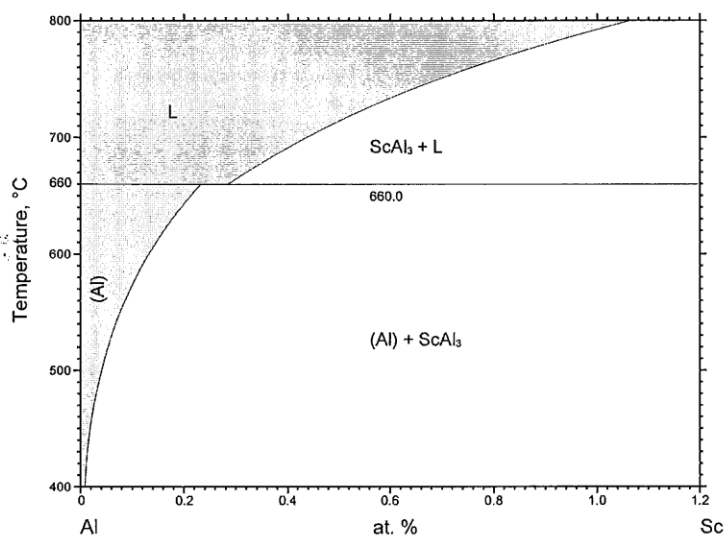
***For Commercial Publications, a copyright permission fee of \$50 per figure will be assessed. Please send check or money order to Permissions at ASM International, 9639 Kinsman Road, Materials Park, Ohio 44073-0002.**

Exceptions can be made for reuse of content by its original authors

Please submit copies or scans of all materials (text, figures, tables) listed in this request.

C:\Users\NICK\Desktop\ASM Copyright Permission Form.doc

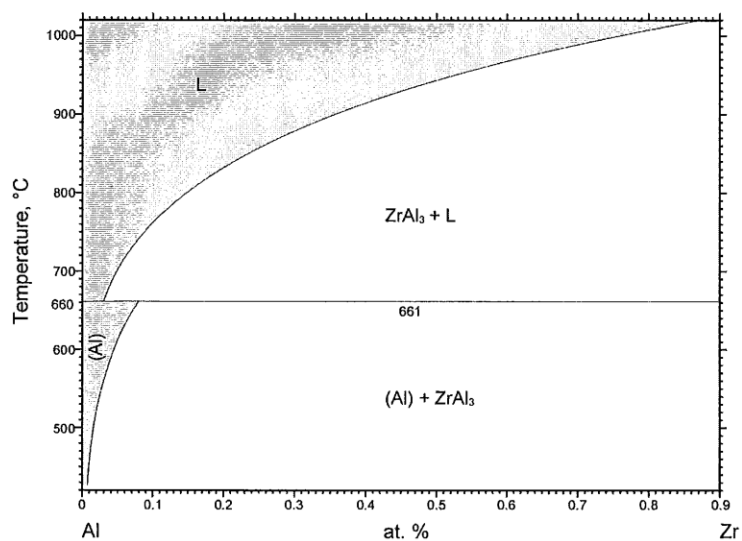
COPYRIGHT PERMISSION REQUEST



© ASM International 2009. Diagram No. 100032

Please submit copies or scans of all materials (text, figures, tables) listed in this request.
 C:\Users\ssellers\AppData\Local\Microsoft\Windows\Temporary Internet Files\Content.Outlook\Y92A7FY5\ASM Copyright Permission Form (27).doc

COPYRIGHT PERMISSION REQUEST



© ASM International 2006. Diagram No. 1600336.

Please submit copies or scans of all materials (text, figures, tables) listed in this request.
 C:\Users\ssellers\AppData\Local\Microsoft\Windows\Temporary Internet Files\Content.Outlook\92A7FYS\ASM Copyright Permission Form (27).doc